

Adaptive Trajectory Tracking Control for the Quadrotor Aerial Transportation System Landing a Payload Onto the Mobile Platform

Hai Yu^{ID}, Student Member, IEEE, Xiao Liang^{ID}, Member, IEEE, Jianda Han^{ID}, Member, IEEE, and Yongchun Fang^{ID}, Senior Member, IEEE

Abstract—Recently, it is becoming increasingly possible to apply aerial transportation systems to real-world applications. However, current research works on cable-suspended transportation systems present practical limitations due to the fixed-length cable. With the introduction of the cable adjustment mechanism, various complicated tasks, such as limited space crossing, offshore sample collection, and even landing the payload on a mobile platform, can be accomplished by actively changing the distance between the quadrotor and the payload. In order to complete the aforementioned tasks, a trajectory tracking control method is in urgent need for the variable-length-cable-suspended aerial transportation systems. To this end, an adaptive tracking control approach with the consideration of unknown resistance coefficients is designed in this article. Subsequently, Lyapunov techniques and Barbalat's Lemma are utilized to prove the convergence for the equilibrium point of the closed-loop system. Finally, hardware experiments are meticulously conducted based on a self-built experimental platform, which verify the satisfactory performance of the proposed method in antiswing aerial transportation and payload landing onto the mobile platform.

Index Terms—Adaptive tracking control, aerial transportation systems, antiswing, payload landing onto the mobile platform, variable-length.

Manuscript received 10 May 2022; revised 16 August 2022 and 15 February 2023; accepted 5 March 2023. Date of publication 13 March 2023; date of current version 11 December 2023. This work was supported in part by the National Natural Science Foundation of China under Grant 62273187, Grant 62233011, and Grant 91848203, in part by the Young Elite Scientists Sponsorship Program by Tianjin under Grant TJSQNTJ-2020-21, and in part by Haihe Lab of ITAI under Grant 22HHXCJC00003. Paper no. TII-22-2015. (Corresponding author: Xiao Liang.)

The authors are with the Institute of Robotics and Automatic Information System, College of Artificial Intelligence, and Tianjin Key Laboratory of Intelligent Robotics, Nankai University, Tianjin 300350, China, and also with the Engineering Research Center of Trusted Behavior Intelligence, Ministry of Education, Nankai University, Tianjin 300350, China (e-mail: yuhai@mail.nankai.edu.cn; liangx@nankai.edu.cn; hanjanda@nankai.edu.cn; fangyc@nankai.edu.cn).

This article has supplementary material provided by the authors and color versions of one or more figures available at <https://doi.org/10.1109/TII.2023.3256374>.

Digital Object Identifier 10.1109/TII.2023.3256374

I. INTRODUCTION

WITH the progress of industrial electronic information technology, robotic techniques develop rapidly [1], [2], [3], [4], [5], [6]. Specially, the quadrotor unmanned aerial vehicle (UAV) has been the research hotspot in the field of robotics [7], [8], [9], [10]. Due to its vertical taking-off and landing ability, hovering capability, lightweight fuselage, and kinematic dexterity, the quadrotor has a broad range of applications, including rescue, photography, delivery, agriculture, etc. [11], [12], [13]. When such natural disasters as earthquakes, floods, forest fires strike, roads become muddy, damaged, or even blocked, thus, it is difficult for ground vehicles to pass through. While quadrotors can considerably improve the efficiency of post-disaster rescue by air for equipment delivery and relief commodities transportation. Therefore, aerial transportation is becoming an important application for quadrotor UAVs.

This article focuses on the cable-suspended aerial transportation system, which is one of the main forms of aerial transportation, and plenty of research works have been done. The quadrotor aerial transportation system is first established to be a differentially flat hybrid system in [14], based on which a vision-based geometric controller is designed for agile flight [15]. Imposing acceleration limitations on the payload, an aggressive payload position and swing angle trajectory generation approach [16] is designed, which makes the transportation system capable of passing through windows and avoiding obstacles. Without iterative optimizations and additional tracking controllers, Xian et al. [17] introduce an online trajectory planning method for quadrotor positioning and payload antiswing. Taking the unknown payload mass caused by rotor downwash force into account, an adaptive controller [18] is designed for payload velocity tracking. To eliminate the steady errors, an integral term is first introduced to the controller in [19], which effectively improves the positioning accuracy of the quadrotor while ensuring the asymptotic stability of the closed-loop system. To deal with unknown wind disturbances, an uncertainty and disturbance estimator-based path-following controller [20] is developed, and the closed-loop system is proved to be asymptotically stable through the reduction theorem. In [21], a smooth dynamic feedback control scheme with guaranteed path invariance is proposed to make the payload converge to the desired path. Based on the fixed-time sliding-mode disturbance observer, Liu et al. [22]

proposed an adaptive hierarchical sliding-mode control scheme for the aerial transportation system, which is able to resist disturbance during flight. Aiming at tracking trajectories accurately and minimizing the payload oscillations, an adaptive neural strictly negative-imaginary control law is designed in [23] for the aerial transportation system to overcome uncertainties during flight. In [24], with the help of the fuzzy-genetic intelligent algorithm, a sliding-mode control scheme is designed to eliminate the chattering phenomenon, which has the ability to deal with inaccurate information about system parameters. In summary, most recent studies [14], [15], [16], [17], [18], [19], [20], [21], [22], [23], [24] mainly focus on the aerial transportation system with fixed-length cable which are not applicable for payload landing mission.

Although there have been numerous control schemes and planning methods for quadrotor transportation systems, the objectives are mainly focused on quadrotor positioning, payload swing elimination, disturbance rejection, and obstacle avoidance, while the payload landing issue is seldom considered. In fact, some studies have been carried out on the landing control of the quadrotor itself [25], [26]. Based on the quadrotor's differential flatness characteristic, a time-optimal trajectory generation approach is provided in [25] to land the quadrotor on a heaving and tilting platform, which is solved by transforming the original planning problem into a nonlinear programming problem. Rodriguez-Ramos et al. [26] are the first to utilize the deep deterministic policy gradients algorithm to solve the landing problem, whose experimental results indicate that the quadrotor can land on the mobile platform with a previously unknown trajectory. Furthermore, visual-based schemes [27], [28], [29] are also widely used for precise landing. Without any external positioning and detection device, a framework for quadrotor localization and mobile platform detection is designed based on computer vision algorithms and multisensor fusion [27]. To realize quadrotor landing on an unknown model mobile platform, a low-complexity position-based visual servoing [28] is designed based on the prescribed performance control technique, which is suitable for quadrotors with low cost and limited computation ability. To restrain parameter uncertainties and external interferences caused by image acquisition and processing, and sensor measurement delays, a robust visual servoing control method is proposed in [29], which presents the better performance compared with the standard visual servoing controller [30].

Recently, some planning methods [31], [32] have been proposed to achieve payload release. However, the throwing method may cause damage to fragile payloads. Facing this practical problem, the recently developed aerial transportation system with variable-length cable [33], [34] is well suited for the payload landing task, which can improve the landing flexibility and keep the quadrotor and the mobile platform at a safe distance. Liang et al. [33] design the first mechanical structure of the aerial transportation system with variable-length cable, which is employed to implement the window crossing and water sampling tasks. In [34], based on the coupling signal between the quadrotor and the payload, an antiswing control method is designed for the system with time-varying cable length. In this article, by fixing an actuator to the quadrotor, the aerial transportation

system with variable-length cable is then utilized to accomplish the objective to land the payload onto the mobile platform. After approaching the mobile platform, the quadrotor remains relatively stationary with respect to the platform and the cable length is extended simultaneously. As the distance between the payload and the mobile platform is close enough, the payload is released. Due to the complex underactuated characteristics of the system, the payload sway motion cannot be suppressed directly. In addition, the unknown resistance coefficient further brings challenges to the platform trajectory tracking, and excessive payload swing will affect the realization of the landing task. Regarding the aforementioned issues, an adaptive trajectory tracking control scheme is designed for the aerial transportation system with variable-length cable, which can track the motion of the mobile target in horizontal space and adjust the cable length in vertical space. Subsequently, the asymptotic convergence of the tracking errors is proved by Lyapunov-based stability analysis and Barbalat's Lemma. Finally, the feasibility of the proposed control scheme is verified by the hardware experiments based on the self-built platform. In order to land the payload onto a mobile platform, the following aspects should be guaranteed: 1) cooperation landing trajectory generation for both the mobile platform and the quadrotor; 2) tracking for the generated trajectory and suppression of the payload swing during transportation and landing. As the planning methods represented by minimum snap algorithm [35] can obtain trajectories suitable for landing tasks, this article mainly focuses on the second aspect. To the best of authors' knowledge, this article presents the first adaptive trajectory tracking control scheme for the aerial transportation system with variable-length cable, which is capable of landing the payload onto the mobile platform. The main contributions of this article can be concluded into the following two aspects.

- 1) *Practical application:* Landing the payload of the aerial transportation system onto a mobile platform is of great significance for practical cargo delivery. However, most existing studies pay more attention to the research of the "transportation process," i.e., the quadrotor transports the payload from the initial position to the desired one. Although some planning methods [31], [32] are proposed to release the payload, the release positions are stationary targets and the throwing method may cause damage to fragile payloads. Besides, despite some research works have been carried out on the landing control of the quadrotor [25], [26], [27], [28], [29], it is difficult to extend these methods to the aerial transportation systems due to the dynamic coupling caused by payload swing. In this article, to facilitate the payload landing mission and make the system more flexible, a cable adjustment mechanism is mounted on the quadrotor to adjust the cable length during the payload release procedure, which avoids potential safety hazards caused by the distance between the quadrotor and the platform. Furthermore, a function demonstration test is detailed to exhibit the system's superior performance in payload landing tasks for mobile platform.
- 2) *Theoretical research:* Compared with the aerial transportation systems with fixed-length cable [14], [15], [16],

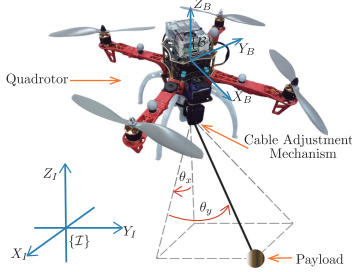


Fig. 1. Quadrotor aerial transportation system with variable-length cable.

TABLE I
SYMBOLS AND DEFINITIONS OF THE SYSTEM

Symbol	Definition
$M \in \mathbb{R}$	Mass of the quadrotor
$m \in \mathbb{R}$	Mass of the payload
$g \in \mathbb{R}$	Gravitational acceleration
$J \in \mathbb{R}^{3 \times 3}$	Quadrotor's moment of inertia
$R \in SO(3)$	Rotation matrix from $\{\mathcal{B}\}$ to $\{\mathcal{I}\}$
$Re_3 = [R_{13}, R_{23}, R_{33}]^\top$	Last column of rotation matrix R
$\xi = [x, y, z]^\top \in \mathbb{R}^3$	Quadrotor position vector
$l \in \mathbb{R}$	Cable length
$\alpha = [\xi^\top, l]^\top \in \mathbb{R}^4$	Combination vector of the quadrotor position and the cable length
$\Theta = [\theta_x, \theta_y]^\top \in \mathbb{R}^2$	Payload swing angle vector
$q = [\alpha^\top, \theta_x, \theta_y]^\top \in \mathbb{R}^6$	Generalized coordinate of the outer loop subsystem
$\xi_p = [x_p, y_p, z_p]^\top \in \mathbb{R}^3$	Payload position vector
$\Omega \in \mathbb{R}^3$	Angular velocity of quadrotor in frame $\{\mathcal{B}\}$
$D_\alpha = \text{diag}([d_x, d_y, d_z, d_l]) \in \mathbb{R}_{+}^{4 \times 4}$	Resistance coefficient matrix of the quadrotor translation and the cable
$d_p \in \mathbb{R}$	Resistance coefficient of the payload
$D_\Omega \in \mathbb{R}_{+}^{3 \times 3}$	Resistance coefficient matrix of the quadrotor rotation
$\alpha_d = [x_d, y_d, z_d, l_d]^\top \in \mathbb{R}^4$	Desired trajectory vector of the quadrotor and the cable
$p_0 = [p_{0x}, p_{0y}, p_{0z}, p_{0l}]^\top \in \mathbb{R}^4$	Initial quadrotor position and cable length vector
$p_f = [p_{fx}, p_{fy}, p_{fz}, p_{fl}]^\top \in \mathbb{R}^4$	Preset final quadrotor position and cable length vector
$R_d \in SO(3)$	Desired rotation matrix
$\Omega_d \in \mathbb{R}^3$	Desired angular velocity of quadrotor
$f \in \mathbb{R}$	Applied thrust scalar generated by quadrotor
$f_t \in \mathbb{R}$	Actuating force generated by the cable adjustment mechanism
$\tau = [\tau_1, \tau_2, \tau_3]^\top \in \mathbb{R}^3$	Torque generated by quadrotor
$f_c = [f_x, f_y, f_z]^\top \in \mathbb{R}^3$	Virtual control input generated by quadrotor
C_x, C_y, S_x, S_y	Abbreviation of $\cos \theta_x, \cos \theta_y, \sin \theta_x$ and $\sin \theta_y$
$M_c(\mathbf{q}) \in \mathbb{R}^{6 \times 6}$	Inertia matrix
$V_c(\mathbf{q}, \dot{\mathbf{q}}) \in \mathbb{R}^{6 \times 6}$	Centrifugal-Coriolis matrix
$G(\mathbf{q}) \in \mathbb{R}^6$	Gravity vector
$F = [fRe_3^\top, f_l, 0, 0] \in \mathbb{R}^6$	Outer loop control input vector
$F_r = [f_{rx}, f_{ry}, f_{rz}, f_{rl}, f_{r\theta_x}, f_{r\theta_y}] \in \mathbb{R}^6$	Resistance force of the system

[17], [18], [19], [20], [21], [22], [23], [24], although the variable-length-cable structure greatly improves the flexibility and the adaptability of the system, it also exhibits stronger nonlinearity, higher degrees of freedom (DOFs) and more complex dynamic coupling due to the variable-length cable dynamics, which leads to significant difficulties in precise control. It is worth mentioning that when the resistance coefficient is unknown, the tracking control of a high-dimensional underactuated system turns into a much more challenging problem. To this end, an adaptive trajectory tracking control scheme is proposed to overcome the aforementioned issues without any linearization operations. Based on the Lyapunov techniques and Barbalat's Lemma, the stability of the closed-loop system is guaranteed. Compared with the literature [33] and [34], this article focuses on the trajectory tracking controller design for the aerial transportation system with variable-length cable and the unknown resistance coefficient is taken into consideration.

The rest of this article is organized as follows. The problem formulation for the aerial transportation system with variable-length cable is established in Section II. Considering the unknown resistance coefficient, Section III provides the

adaptive tracking controller design and stability analysis. In Section IV, simulation and experimental results are provided to show the performance of the control system. Finally, Section V concludes this article.

II. PROBLEM FORMULATION

The schematic of the quadrotor aerial transportation system with variable-length cable is shown in Fig. 1, whose cable length is changed through an adjustment mechanism composed of a spool, an actuator, and a connector. The spool is connected to the actuator via the connector, and the actuator provides the power to turn the spool, thus the cable length can be changed. $\{\mathcal{I}\}$ and $\{\mathcal{B}\}$ represent the right-hand inertia frame and the body-fixed frame, respectively. Table I lists the utilized symbols and their corresponding definitions. Considering the actual characteristics of the cable-suspended transportation systems, the following reasonable assumptions are given [16], [17], [18], [20], [36]:

Assumption 1: The suspension cable is inelastic and massless, whose length is greater than zero and less than the preset maximum length \bar{l} , i.e., $0 < l < \bar{l}$.

Assumption 2: The payload is always under the quadrotor, implying that the swing angles θ_x and θ_y are within the range of $(-\pi/2, \pi/2)$.

Assumption 3: The suspension point of the cable is located at the quadrotor's center of gravity.

A. Dynamics of the Quadrotor Aerial Transportation System With Variable-Length Cable

The dynamic model is divided into two subsystems. The inner loop subsystem is the rotation of the quadrotor, the outer loop subsystem is composed of the quadrotor translation, cable length variation, and payload swing angles. According to the geometric relations between the quadrotor and the payload, the payload's position can be expressed as $\xi_p = \xi + l[S_x C_y, S_y, -C_x C_y]^\top$. The Lagrangian of the outer loop subsystem is $L = 1/2M\dot{\xi}^\top \dot{\xi} + 1/2m\dot{\xi}_p^\top \dot{\xi}_p - (Mgz + mgz_p)$. The generalized force is $Q_i = \delta W / \delta q_i, i = \{1, \dots, 6\}$, where δq_i is the virtual displacement and $\delta W = ([fRe_3^\top, f_l]^\top + f_c)^\top \delta \alpha + f_p^\top \delta \xi_p$ is the virtual work, $f_c = -D_\alpha \dot{\alpha}$ and $f_p = -d_p \dot{\xi}_p$ are the resistance forces. Subsequently, based on the Lagrange's equation $\frac{d}{dt} \frac{\partial L}{\partial \dot{q}_i} - \frac{\partial L}{\partial q_i} = Q_i$, the dynamics of the outer loop subsystem can be established as

$$(M+m)\ddot{x} + ml\ddot{\theta}_x C_x C_y + 2ml\dot{\theta}_x C_x C_y - 2ml\dot{\theta}_y S_x S_y \\ + ml(\ddot{\theta}_x C_x C_y - \ddot{\theta}_y S_x S_y - \dot{\theta}_x^2 S_x C_y - \dot{\theta}_y^2 S_x C_y \\ - 2\dot{\theta}_x \dot{\theta}_y C_x S_y) = f_{R13} + f_{rx} \quad (1)$$

$$(M+m)\ddot{y} + ml\ddot{\theta}_y C_y + 2ml\dot{\theta}_y C_y + ml(\ddot{\theta}_y C_y - \dot{\theta}_y^2 S_y) \\ = f_{R23} + f_{ry} \quad (2)$$

$$(M+m)\ddot{z} - ml\ddot{C}_x C_y + 2ml\dot{\theta}_x S_x C_y + 2ml\dot{\theta}_y C_x S_y \\ + ml(\ddot{\theta}_x S_x C_y + \ddot{\theta}_y C_x S_y + \dot{\theta}_x^2 C_x C_y + \dot{\theta}_y^2 C_x C_y \\ - 2\dot{\theta}_x \dot{\theta}_y S_x S_y) + (M+m)g = f_{R33} + f_{rz} \quad (3)$$

$$\begin{aligned} m\ddot{x}S_xC_y + m\ddot{y}S_y - m\ddot{z}C_xC_y + ml\ddot{l} - ml\dot{\theta}_x^2C_y^2 - ml\dot{\theta}_y^2 \\ - mgC_xC_y = f_l + f_{rl} \end{aligned} \quad (4)$$

$$\begin{aligned} ml\ddot{x}C_xC_y + ml\ddot{z}S_xC_y + ml^2\ddot{\theta}_x^2C_y^2 + 2ml\dot{l}\dot{\theta}_xC_y^2 \\ - 2ml^2\dot{\theta}_x\dot{\theta}_yC_y + mglS_xC_y = f_{r\theta_x} \end{aligned} \quad (5)$$

$$\begin{aligned} - ml\ddot{x}S_xS_y + ml\ddot{y}C_y + ml\ddot{z}C_xS_y + ml^2\ddot{\theta}_y + 2ml\dot{l}\dot{\theta}_y \\ + ml^2\dot{\theta}_x^2C_yS_y + mglC_xS_y = f_{r\theta_y} \end{aligned} \quad (6)$$

where $f_{rx} = -d_x\dot{x} - d_p(\dot{x} + lS_xC_y + l\dot{\theta}_xC_xC_y - l\dot{\theta}_yS_xS_y)$, $f_{ry} = -d_y\dot{y} - d_p(\dot{y} + lS_y + l\dot{\theta}_yC_y)$, $f_{rz} = -d_z\dot{z} - d_p(\dot{z} - lC_xC_y + l\dot{\theta}_xS_xC_y + l\dot{\theta}_yC_xS_y)$, $f_{rl} = -d_l\dot{l} - d_p\dot{l} - d_p\dot{x}S_xC_y - d_p\dot{y}S_y + d_p\dot{z}C_xC_y$, $f_{r\theta_x} = -d_p(l(\dot{x}C_x + l\dot{\theta}_xC_y + \dot{z}S_x)C_y)$, $f_{r\theta_y} = -d_p(l(-\dot{x}S_xS_y + \dot{y}C_y + \dot{z}C_xS_y + l\dot{\theta}_y))$, and (1)–(6) can be written in a compact form as¹

$$M_c(\mathbf{q})\ddot{\mathbf{q}} + V_c(\mathbf{q}, \dot{\mathbf{q}})\dot{\mathbf{q}} + \mathbf{G}(\mathbf{q}) = \mathbf{F} + \mathbf{F}_r. \quad (7)$$

Besides, according to Assumption 3, the rotational dynamics of the quadrotor is not influenced by the payload. Thus, the inner loop subsystem stays the same as the quadrotor, which is expressed by

$$\dot{R} = R\mathbf{s}\kappa(\boldsymbol{\Omega}) \quad (8)$$

$$J\dot{\boldsymbol{\Omega}} + \mathbf{s}\kappa(\boldsymbol{\Omega})J\boldsymbol{\Omega} = \boldsymbol{\tau} - D_\Omega\boldsymbol{\Omega} \quad (9)$$

where $\mathbf{s}\kappa(\cdot) : \mathbb{R}^3 \rightarrow \mathfrak{so}(3)$ is defined by the relation that $\mathbf{s}\kappa(\mathbf{x})\mathbf{y} = \mathbf{x} \times \mathbf{y}$ for all $\mathbf{x}, \mathbf{y} \in \mathbb{R}^3$. $\text{vex}(\cdot) : \mathfrak{so}(3) \rightarrow \mathbb{R}^3$ is the inverse operation of $\mathbf{s}\kappa(\cdot)$. Thus, the complete model of the system can be summarized by (7)–(9). Analogous to many other Euler–Lagrange systems [37], [38], [39], one can verify that model (7) satisfies the following property.

Property 1: M_c and V_c satisfy the skew-symmetric relationship, i.e., $\chi^\top (\frac{1}{2}M_c - V_c)\chi = 0$, $\forall \chi \in \mathbb{R}^6$.

Remark 1: Based on the dynamic model of the aerial transportation system with variable-length cable (7)–(9), one can find that there are nine DOFs including three quadrotor position DOFs, one cable length DOF, two payload swing angle DOFs, and three quadrotor rotation DOFs. In addition, there are five control inputs including a quadrotor thrust and three torques, and a cable length adjustment force.

B. Control Objective

For the cooperation payload landing task, the control objective is to design a feedback control law that drives the quadrotor and the cable to track the desired trajectory vector $\boldsymbol{\alpha}_d(t)$ and finally reach the preset final position \mathbf{p}_d , while suppressing the payload swing during the process. Besides, the mobile platform's trajectory is the same as the quadrotor in horizontal plane. Thus, the objective can be quantified as

$$\boldsymbol{\alpha}(t) \rightarrow \boldsymbol{\alpha}_d(t) \Rightarrow \lim_{t \rightarrow \infty} \boldsymbol{\alpha}(t) = \mathbf{p}_d, \boldsymbol{\Theta} \rightarrow [0, 0]^\top \quad (10)$$

¹Combined with Assumption 2, M_c is proved to be positive definite by calculating the leading principal submatrices.

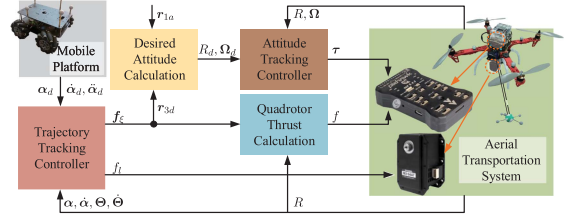


Fig. 2. Structure of the overall control system.

where the desired trajectory vector $\boldsymbol{\alpha}_d(t)$ is selected based on the following property.

Property 2: The desired trajectory $\boldsymbol{\alpha}_d(t)$ gradually converges from the initial position \mathbf{p}_0 to the preset final position \mathbf{p}_d as time goes on, and its time derivatives satisfy $|\dot{\boldsymbol{\alpha}}_d(t)| \leq \bar{v}$, $|\ddot{\boldsymbol{\alpha}}_d(t)| \leq \bar{a}$, $|\boldsymbol{\alpha}_d^{(3)}(t)| \leq \bar{j}$, where $\bar{v}, \bar{a}, \bar{j}$ are positive upper bound constant vectors.² $\dot{\boldsymbol{\alpha}}_d(t)$ and $\ddot{\boldsymbol{\alpha}}_d(t)$ are square integrable, i.e., $\dot{\boldsymbol{\alpha}}_d(t), \ddot{\boldsymbol{\alpha}}_d(t) \in \mathcal{L}_2$. For the convenience of payload landing, the cable length is extended during the mission, i.e., $\dot{l}_d \geq 0$.

Remark 2: This article mainly deals with the payload landing problem, thus, the cable length trajectory is selected to satisfy $\dot{l}_d \geq 0$. It is also the key point for the subsequent theoretical analysis. In future efforts, we will concentrate on designing more advanced control schemes that are applicable to unrestrained cable length velocity \dot{l}_d .

As presented in Property 2, one can find that³

$$\dot{\boldsymbol{\alpha}}_d(t), \ddot{\boldsymbol{\alpha}}_d(t), \boldsymbol{\alpha}_d^{(3)}(t) \in \mathcal{L}_\infty, \dot{\boldsymbol{\alpha}}_d(t), \ddot{\boldsymbol{\alpha}}_d(t) \in \mathcal{L}_2. \quad (11)$$

By invoking the Barbalat's Lemma, one can get

$$\begin{aligned} \lim_{t \rightarrow \infty} \dot{\boldsymbol{\alpha}}_d(t) &= \mathbf{0}_{4 \times 1}, \lim_{t \rightarrow \infty} \ddot{\boldsymbol{\alpha}}_d(t) = \mathbf{0}_{4 \times 1} \Rightarrow \\ \lim_{t \rightarrow \infty} \dot{x}_d(t) &= \lim_{t \rightarrow \infty} \dot{y}_d(t) = \lim_{t \rightarrow \infty} \dot{z}_d(t) = \lim_{t \rightarrow \infty} \dot{l}_d(t) = 0 \\ \lim_{t \rightarrow \infty} \ddot{x}_d(t) &= \lim_{t \rightarrow \infty} \ddot{y}_d(t) = \lim_{t \rightarrow \infty} \ddot{z}_d(t) = \lim_{t \rightarrow \infty} \ddot{l}_d(t) = 0. \end{aligned} \quad (12)$$

III. MAIN RESULTS

In this section, considering the unknown resistance coefficients in the transportation process, an adaptive tracking controller is designed for the quadrotor aerial transportation system. Fig. 2 presents the control structure of the overall system.

A. Controller Design

According to the control objective (10), the system's error signal vector is defined as

$$\mathbf{e}(t) = [\mathbf{e}_\alpha^\top, \theta_x, \theta_y]^\top = [\boldsymbol{\alpha}^\top - \boldsymbol{\alpha}_d^\top, \theta_x, \theta_y]^\top$$

$$\mathbf{e}_R = \frac{1}{2} \text{vex} (R_d^\top R - R^\top R_d), \mathbf{e}_\Omega = \boldsymbol{\Omega} - R^\top R_d \boldsymbol{\Omega}_d.$$

²Notations $\succ, \prec, \succeq, \preceq$ are used to denote element-wise vector inequalities.

³If the ∞ norm of v satisfies $\|v\|_\infty \leq \infty$, then we say that v belongs to \mathcal{L}_∞ , i.e., $v \in \mathcal{L}_\infty$ [40].

Subsequently, based on the energy form of the system, a positive definite function is constructed as follows:

$$V_1 = \frac{1}{2} \dot{\mathbf{e}}^\top M_c \dot{\mathbf{e}} + mgl(1 - C_x C_y) + \frac{1}{2} \mathbf{e}_\alpha^\top K_p \mathbf{e}_\alpha \quad (13)$$

where $K_p = \text{diag}([k_{px}, k_{py}, k_{pz}, k_{pl}]) \in \mathbb{R}_+^{4 \times 4}$ is a positive definite diagonal matrix. According to Property 1, inserting (7) into the time derivative of V_1 , one can obtain the following result:

$$\begin{aligned} \dot{V}_1 &= \dot{\mathbf{e}}^\top \left(M_c \ddot{\mathbf{e}} + \frac{1}{2} \dot{M}_c \dot{\mathbf{e}} \right) + mgl \left(\dot{\theta}_x S_x C_y + \dot{\theta}_y C_x S_y \right) \\ &\quad + mgl(1 - C_x C_y) + \dot{\mathbf{e}}_\alpha^\top K_p \mathbf{e}_\alpha \\ &= \dot{\mathbf{e}}^\top \left(\mathbf{F} + \mathbf{F}_r - \mathbf{G} - V_c \dot{\mathbf{q}}_d - M_c \ddot{\mathbf{q}}_d - V_c \dot{\mathbf{e}} + \frac{1}{2} \dot{M}_c \dot{\mathbf{e}} \right) + \dot{\mathbf{e}}_\alpha^\top K_p \mathbf{e}_\alpha \\ &\quad + mgl(1 - C_x C_y) + mgl \left(\dot{\theta}_x S_x C_y + \dot{\theta}_y C_x S_y \right) \\ &= \dot{\mathbf{e}}^\top \left(\mathbf{F} + \mathbf{F}_r - V_c \dot{\mathbf{q}}_d - M_c \ddot{\mathbf{q}}_d - V_c \dot{\mathbf{e}} + \frac{1}{2} \dot{M}_c \dot{\mathbf{e}} \right) - \dot{\mathbf{e}}_x \cdot 0 - \dot{\mathbf{e}}_y \cdot 0 \\ &\quad - (M+m)g \dot{\mathbf{e}}_z + mg \dot{\mathbf{e}}_l C_x C_y - mgl \dot{\theta}_x S_x C_y - mgl \dot{\theta}_y C_x S_y \\ &\quad + \dot{\mathbf{e}}_\alpha^\top K_p \mathbf{e}_\alpha + mgl(1 - C_x C_y) + mgl \left(\dot{\theta}_x S_x C_y + \dot{\theta}_y C_x S_y \right) \\ &= \dot{\mathbf{e}}_\alpha^\top \mathbf{N} - \dot{\mathbf{e}}_\alpha^\top \Phi_\omega + \dot{\mathbf{e}}_\alpha^\top K_p \mathbf{e}_\alpha + mg(1 - C_x C_y) \dot{l}_d \\ &\quad - l \dot{\theta}_y C_y (m \ddot{y}_d + d_p \dot{y}_d) - l \left(\dot{\theta}_x^2 C_y^2 + \dot{\theta}_y^2 \right) (m \ddot{l}_d + d_p \dot{l}_d) \\ &\quad - l \left(\dot{\theta}_x C_x C_y - \dot{\theta}_y S_x S_y \right) (m \ddot{x}_d + d_p \dot{x}_d) \\ &\quad - l \left(\dot{\theta}_x C_y S_x + \dot{\theta}_y C_x S_y \right) (m \ddot{z}_d + d_p \dot{z}_d) \end{aligned} \quad (14)$$

wherein vector \mathbf{N} and vector Φ_ω are arranged as follows:

$$\mathbf{N} =$$

$$\begin{bmatrix} f R_{13} - (M+m) \ddot{x}_d - m \left(S_x C_y \ddot{l}_d + \left(\dot{\theta}_x C_x C_y - \dot{\theta}_y S_x S_y \right) \dot{l}_d \right) \\ f R_{23} - (M+m) \ddot{y}_d - m S_y \ddot{l}_d - m \dot{\theta}_y C_y \dot{l}_d \\ f R_{33} - (M+m)(g+z_d) + m \left(C_x C_y \ddot{l}_d - \left(\dot{\theta}_x C_y S_x + \dot{\theta}_y C_x S_y \right) \dot{l}_d \right) \\ f_l - m \ddot{l}_d - m S_x C_y \ddot{x}_d - m S_y \ddot{y}_d + m C_x C_y \ddot{z}_d + mg \end{bmatrix}$$

$$\Phi_\omega = [\phi_x^\top \omega_x, \phi_y^\top \omega_y, \phi_z^\top \omega_z, \phi_l^\top \omega_l]^\top$$

and the composite velocity signal vectors $\phi_x, \phi_y, \phi_z, \phi_l \in \mathbb{R}^2$ as well as the resistance coefficient vectors $\omega_x, \omega_y, \omega_z, \omega_l \in \mathbb{R}^2$ in Φ_ω are represented as

$$\begin{aligned} \omega_x &= [d_x + d_p, d_p]^\top, \omega_y = [d_y + d_p, d_p]^\top, \omega_z = [d_z + d_p, d_p]^\top \\ \omega_l &= [d_l + d_p, d_p]^\top, \phi_x = \left[\dot{x}, \dot{l} S_x C_y + 2l \left(\dot{\theta}_x C_x C_y - \dot{\theta}_y S_x S_y \right) \right]^\top \\ \phi_y &= \left[\dot{y}, \dot{l} S_y + 2l \dot{\theta}_y C_y \right]^\top, \phi_l = \left[\dot{l}, S_x C_y \dot{x} + S_y \dot{y} - C_x C_y \dot{z} \right]^\top \\ \phi_z &= \left[\dot{z}, -l C_x C_y + 2l \left(\dot{\theta}_x C_y S_x + \dot{\theta}_y C_x S_y \right) \right]^\top. \end{aligned}$$

For the sake of description, (14) can be further written as

$$\begin{aligned} \dot{V}_1 &= \dot{\mathbf{e}}_\alpha^\top (\mathbf{u} + \mathbf{u}_\Delta - M \mathbf{\Xi}_d - m \mathbf{\Psi}_d - \Phi_\omega + K_p \mathbf{e}_\alpha) \\ &\quad + mg(1 - C_x C_y) \dot{l}_d - l \left(\dot{\theta}_x C_x C_y - \dot{\theta}_y S_x S_y \right) (m \ddot{x}_d + d_p \dot{x}_d) \end{aligned}$$

$$\begin{aligned} &- l \dot{\theta}_y C_y (m \ddot{y}_d + d_p \dot{y}_d) - l \left(\dot{\theta}_x^2 C_y^2 + \dot{\theta}_y^2 \right) (m \ddot{l}_d + d_p \dot{l}_d) \\ &- l \left(\dot{\theta}_x C_y S_x + \dot{\theta}_y C_x S_y \right) (m \ddot{z}_d + d_p \dot{z}_d) \end{aligned} \quad (15)$$

where vector $\mathbf{\Xi}_d$ and $\mathbf{\Psi}_d$ take the following form as

$$\mathbf{\Xi}_d = [\ddot{x}_d, \ddot{y}_d, \ddot{z}_d + g, 0]^\top$$

$$\mathbf{\Psi}_d = \begin{bmatrix} \ddot{x}_d + S_x C_y \ddot{l}_d + \left(\dot{\theta}_x C_x C_y - \dot{\theta}_y S_x S_y \right) \dot{l}_d \\ \ddot{y}_d + S_y \ddot{l}_d + \dot{\theta}_y C_y \dot{l}_d \\ \ddot{z}_d - C_x C_y \ddot{l}_d + \left(\dot{\theta}_x C_y S_x + \dot{\theta}_y C_x S_y \right) \dot{l}_d + g \\ \ddot{l}_d + S_x C_y \ddot{x}_d + S_y \ddot{y}_d - C_x C_y \ddot{z}_d - g \end{bmatrix}$$

the constructed virtual control input $\mathbf{u} = [\mathbf{f}_\xi^\top, f_l]^\top \in \mathbb{R}^4$ and the auxiliary vector $\mathbf{u}_\Delta = [\mathbf{f}_\Delta^\top, 0]^\top \in \mathbb{R}^4$ satisfies $\mathbf{u} + \mathbf{u}_\Delta = [\mathbf{f}_\xi^\top, f_l]^\top + [\mathbf{f}_\Delta^\top, 0]^\top = [\mathbf{f}^\top R_d e_3^\top, f_l]^\top$. $\mathbf{f}_\xi \in \mathbb{R}^3$ and $\mathbf{f}_\Delta \in \mathbb{R}^3$ are given as $\mathbf{f}_\xi = \frac{f}{e_3^\top R_d^\top R e_3} R_d e_3$, $\mathbf{f}_\Delta = \frac{f}{e_3^\top R_d^\top R e_3} [(e_3^\top R_d^\top R e_3) R e_3 - R_d e_3]$. Vector \mathbf{f}_Δ reflects the coupling between the quadrotor's translation and rotation.

Thus, combined with the result in (15), the following controller is designed elaborately:

$$\mathbf{u} = -K_p \mathbf{e}_\alpha - K_d \dot{\mathbf{e}}_\alpha + M \mathbf{\Xi}_d + m \mathbf{\Psi}_d + \hat{\Phi}_\omega \quad (16)$$

where $K_d = \text{diag}([k_{dx}, k_{dy}, k_{dz}, k_{dl}]) \in \mathbb{R}_+^{4 \times 4}$ is a positive definite diagonal control gain matrix and $\hat{\Phi}_\omega = [\phi_x^\top \hat{\omega}_x, \phi_y^\top \hat{\omega}_y, \phi_z^\top \hat{\omega}_z, \phi_l^\top \hat{\omega}_l]^\top$ is the to-be-designed online estimation of Φ_ω . The online update rates for the resistance coefficient vectors are designed as

$$\begin{aligned} \dot{\hat{\omega}}_x &= -\Gamma_x \phi_x \dot{\epsilon}_x, \dot{\hat{\omega}}_y = -\Gamma_y \phi_y \dot{\epsilon}_y, \\ \dot{\hat{\omega}}_z &= -\Gamma_z \phi_z \dot{\epsilon}_z, \dot{\hat{\omega}}_l = -\Gamma_l \phi_l \dot{\epsilon}_l \end{aligned} \quad (17)$$

where $\Gamma_x = \text{diag}([\gamma_{x1}, \gamma_{x2}]) \in \mathbb{R}_+^{2 \times 2}$, $\Gamma_y = \text{diag}([\gamma_{y1}, \gamma_{y2}]) \in \mathbb{R}_+^{2 \times 2}$, $\Gamma_z = \text{diag}([\gamma_{z1}, \gamma_{z2}]) \in \mathbb{R}_+^{2 \times 2}$, $\Gamma_l = \text{diag}([\gamma_{l1}, \gamma_{l2}]) \in \mathbb{R}_+^{2 \times 2}$ are diagonal gain matrices with positive parameters.

Subsequently, according to the relation $\mathbf{f}_\xi = \frac{f}{e_3^\top R_d^\top R e_3} R_d e_3$, one can find that \mathbf{f}_ξ and $R_d e_3$ have the same direction, then the desired unit direction vector $r_{3d} = R_d e_3 \in \mathbb{R}^3$ can be obtained by $r_{3d} = R_d e_3 = \frac{f_\xi}{\|f_\xi\|}$. Thus, \mathbf{f}_ξ can be further arranged as

$$\mathbf{f}_\xi = \frac{f \|f_\xi\|}{f_\xi^\top R e_3} \cdot \frac{f_\xi}{\|f_\xi\|} = \frac{f \cdot f_\xi}{f_\xi^\top R e_3} \Rightarrow \mathbf{f}_\xi^\top R e_3 \cdot \mathbf{f}_\xi = f \cdot f_\xi$$

which indicates that

$$f = \mathbf{f}_\xi^\top R e_3. \quad (18)$$

Besides, on the basis of the obtained unit vector r_{3d} , selecting an arbitrary vector $r_{1a}(t) \in \mathbb{R}^3$ not parallel to r_{3d} , one can calculate the desired attitude as $R_d(t) = [r_{2d} \times r_{3d}; r_{2d}; r_{3d}]$, where $r_{2d} = \frac{r_{3d} \times r_{1a}}{\|r_{3d} \times r_{1a}\|}$ represents the second row of the desired rotation matrix. According to the geometric controller design method [41], the adaptive attitude tracking controller is given as follows:

$$\begin{aligned} \boldsymbol{\tau} &= -k_R \mathbf{e}_R - k_\Omega \mathbf{e}_\Omega + \hat{D}_\Omega \boldsymbol{\Omega} + J R^\top R_d \dot{\boldsymbol{\Omega}}_d \\ &\quad + \text{sk}(R^\top R_d \boldsymbol{\Omega}_d) J R^\top R_d \boldsymbol{\Omega}_d \end{aligned} \quad (19)$$

where $k_R, k_\Omega \in \mathbb{R}_+$ are positive gain constants, \hat{D}_Ω is the estimation of D_Ω . Under the control scheme (19), e_R and e_Ω converge to zero asymptotically.

B. Theoretical Analysis

Based on the abovementioned work, the following theorem can be obtained.

Theorem 1: The proposed control law (16) and update law (17) guarantee that the tracking error of the outerloop system converge to zero, i.e.,

$$\lim_{t \rightarrow \infty} [e_\alpha^\top, \Theta^\top, \dot{e}_\alpha^\top, \dot{\Theta}^\top]^\top = [\mathbf{0}_{4 \times 1}^\top, \mathbf{0}_{2 \times 1}^\top, \mathbf{0}_{4 \times 1}^\top, \mathbf{0}_{2 \times 1}^\top]^\top.$$

Proof: Based on the idea of hierarchical control [42], [43], the coupling term f_Δ can be temporarily neglected, thus, the auxiliary vector turns $\mathbf{u}_\Delta = \mathbf{0}_{4 \times 1}$. To prove Theorem 1, on the basis of (13), choose the Lyapunov candidate function as

$$V_2 = V_1 + \frac{1}{2} \tilde{\omega}_x^\top \Gamma_x^{-1} \tilde{\omega}_x + \frac{1}{2} \tilde{\omega}_y^\top \Gamma_y^{-1} \tilde{\omega}_y + \frac{1}{2} \tilde{\omega}_z^\top \Gamma_z^{-1} \tilde{\omega}_z + \frac{1}{2} \tilde{\omega}_l^\top \Gamma_l^{-1} \tilde{\omega}_l \quad (20)$$

where $\tilde{\omega}_x = \omega_x - \hat{\omega}_x$, $\tilde{\omega}_y = \omega_y - \hat{\omega}_y$, $\tilde{\omega}_z = \omega_z - \hat{\omega}_z$, and $\tilde{\omega}_l = \omega_l - \hat{\omega}_l$ are estimation errors, thus, one can derive that

$$\dot{\tilde{\omega}}_x = -\dot{\hat{\omega}}_x, \dot{\tilde{\omega}}_y = -\dot{\hat{\omega}}_y, \dot{\tilde{\omega}}_z = -\dot{\hat{\omega}}_z, \dot{\tilde{\omega}}_l = -\dot{\hat{\omega}}_l. \quad (21)$$

Subsequently, substituting (16) and (21) into the time derivative of (20) yields

$$\begin{aligned} \dot{V}_2 = & -k_{dx}\dot{e}_x^2 - k_{dy}\dot{e}_y^2 - k_{dz}\dot{e}_z^2 - k_{dl}\dot{e}_l^2 + mg(1 - C_x C_y)\dot{l}_d \\ & - l(\dot{\theta}_x C_x C_y - \dot{\theta}_y S_x S_y)(m\ddot{x}_d + d_p \dot{x}_d) - l\dot{\theta}_y C_y(m\ddot{y}_d + d_p \dot{y}_d) \\ & + d_p l^2 \dot{\theta}_x^2 C_x^2 C_y^2 + d_p l^2 \dot{\theta}_y^2 S_x^2 S_y^2 \\ & - l(\dot{\theta}_x^2 C_y^2 + \dot{\theta}_y^2)(m\dot{l}_d + d_p l). \end{aligned} \quad (22)$$

According to Young's inequality, the following conclusions are obtained:

$$\begin{aligned} -l\dot{\theta}_x C_x C_y (m\ddot{x}_d + d_p \dot{x}_d) &\leq \frac{d_p l^2 \dot{\theta}_x^2 C_x^2 C_y^2}{2} + \frac{(m\ddot{x}_d + d_p \dot{x}_d)^2}{2d_p} \\ l\dot{\theta}_y S_x S_y (m\ddot{x}_d + d_p \dot{x}_d) &\leq \frac{d_p l^2 \dot{\theta}_y^2 S_x^2 S_y^2}{2} + \frac{(m\ddot{x}_d + d_p \dot{x}_d)^2}{2d_p} \\ -l\dot{\theta}_y C_y (m\ddot{y}_d + d_p \dot{y}_d) &\leq \frac{d_p l^2 \dot{\theta}_y^2 C_y^2}{2} + \frac{(m\ddot{y}_d + d_p \dot{y}_d)^2}{2d_p} \\ -l\dot{\theta}_x S_x C_y (m\ddot{z}_d + d_p \dot{z}_d) &\leq \frac{d_p l^2 \dot{\theta}_x^2 S_x^2 C_y^2}{2} + \frac{(m\ddot{z}_d + d_p \dot{z}_d)^2}{2d_p} \\ -l\dot{\theta}_y C_x S_y (m\ddot{z}_d + d_p \dot{z}_d) &\leq \frac{d_p l^2 \dot{\theta}_y^2 C_x^2 S_y^2}{2} + \frac{(m\ddot{z}_d + d_p \dot{z}_d)^2}{2d_p}. \end{aligned}$$

Besides, based on Property 2 and Assumption 1, one can obtain that $-m\dot{l}_d(\dot{\theta}_x^2 C_y^2 + \dot{\theta}_y^2) \leq 0$. Thus, employing the abovementioned inequations and the mathematical relationship

$0 \leq 1 - C_x C_y \leq 2$, (22) is reduced to

$$\begin{aligned} \dot{V}_2 \leq & -k_{dx}\dot{e}_x^2 - k_{dy}\dot{e}_y^2 - k_{dz}\dot{e}_z^2 - k_{dl}\dot{e}_l^2 + 2mg\dot{l}_d + \frac{(m\ddot{x}_d + d_p \dot{x}_d)^2}{d_p} \\ & + \frac{(m\ddot{y}_d + d_p \dot{y}_d)^2}{2d_p} + \frac{(m\ddot{z}_d + d_p \dot{z}_d)^2}{d_p} + \frac{d_p l^2 \dot{\theta}_x^2 C_x^2 C_y^2}{2} \\ & + \frac{d_p l^2 \dot{\theta}_y^2 S_x^2 S_y^2}{2} + \frac{d_p l^2 \dot{\theta}_y^2 C_y^2}{2} + \frac{d_p l^2 \dot{\theta}_x^2 S_x^2 C_y^2}{2} + \frac{d_p l^2 \dot{\theta}_y^2 C_x^2 S_y^2}{2} \\ & - d_p l^2 (\dot{\theta}_x^2 C_y^2 + \dot{\theta}_y^2) - m\dot{l}_d (\dot{\theta}_x^2 C_y^2 + \dot{\theta}_y^2) \\ \leq & -k_{dx}\dot{e}_x^2 - k_{dy}\dot{e}_y^2 - k_{dz}\dot{e}_z^2 - k_{dl}\dot{e}_l^2 + 2mg\dot{l}_d \\ & + \frac{(m\ddot{x}_d + d_p \dot{x}_d)^2}{d_p} + \frac{(m\ddot{y}_d + d_p \dot{y}_d)^2}{2d_p} + \frac{(m\ddot{z}_d + d_p \dot{z}_d)^2}{d_p} \\ & - \frac{1}{2} d_p l^2 (\dot{\theta}_x^2 C_y^2 + \dot{\theta}_y^2). \end{aligned} \quad (23)$$

Subsequently, integrating (23) with respect to time and noticing Assumption 1, one has

$$\begin{aligned} V_2(t) \leq & V_2(0) - k_{dx} \int_0^t \dot{e}_x^2 d\tau - k_{dy} \int_0^t \dot{e}_y^2 d\tau - k_{dz} \int_0^t \dot{e}_z^2 d\tau \\ & - k_{dl} \int_0^t \dot{e}_l^2 d\tau + \int_0^t \frac{(m\ddot{x}_d + d_p \dot{x}_d)^2}{d_p} d\tau \\ & + \int_0^t \frac{(m\ddot{y}_d + d_p \dot{y}_d)^2}{2d_p} d\tau + \int_0^t \frac{(m\ddot{z}_d + d_p \dot{z}_d)^2}{d_p} d\tau \\ & - \frac{1}{2} d_p l^2 \int_0^t (\dot{\theta}_x^2 C_y^2 + \dot{\theta}_y^2) d\tau + 2mg [l_d(t) - l_d(0)] \\ \leq & V_2(0) + \int_0^t \frac{(m\ddot{x}_d + d_p \dot{x}_d)^2}{d_p} d\tau + \int_0^t \frac{(m\ddot{y}_d + d_p \dot{y}_d)^2}{2d_p} d\tau \\ & + \int_0^t \frac{(m\ddot{z}_d + d_p \dot{z}_d)^2}{d_p} d\tau + 2mg\bar{l}. \end{aligned} \quad (24)$$

Then, on the basis of Young's inequality and the fact $V_2(0) \ll +\infty$, $V_2(t)$ can be further deduced as

$$\begin{aligned} V_2(t) \leq & V_2(0) + \left(\frac{m^2}{d_p} + m \right) \int_0^t \ddot{x}_d^2 d\tau + (d_p + m) \int_0^t \dot{x}_d^2 d\tau \\ & + \left(\frac{m^2}{2d_p} + \frac{m}{2} \right) \int_0^t \ddot{y}_d^2 d\tau + \frac{d_p + m}{2} \int_0^t \dot{y}_d^2 d\tau \\ & + \left(\frac{m^2}{d_p} + m \right) \int_0^t \ddot{z}_d^2 d\tau + (d_p + m) \int_0^t \dot{z}_d^2 d\tau \\ & + 2mg\bar{l} \ll +\infty \end{aligned} \quad (25)$$

where the property $\dot{\alpha}_d(t), \ddot{\alpha}_d(t) \in \mathcal{L}_2$ is utilized and indicates that

$$\begin{aligned} V_2 \in \mathcal{L}_\infty \Rightarrow & e_x, e_y, e_z, e_l, \theta_x, \theta_y, \dot{e}_x, \dot{e}_y, \dot{e}_z, \dot{e}_l, \dot{\theta}_x, \dot{\theta}_y, \in \mathcal{L}_\infty \\ \tilde{\omega}_x, \tilde{\omega}_y, \tilde{\omega}_z, \tilde{\omega}_l \in \mathcal{L}_\infty \Rightarrow & \dot{x}, \dot{y}, \dot{z}, \dot{l} \in \mathcal{L}_\infty \\ \Rightarrow & f_{rx}, f_{ry}, f_{rz}, f_{rl}, f_{r\theta_x}, f_{r\theta_y}, \mathbf{u} \in \mathcal{L}_\infty. \end{aligned} \quad (26)$$

Then, combining with the system model (1)–(6) and (12) yields

$$\ddot{x}, \ddot{y}, \ddot{z}, \ddot{l}, \ddot{\theta}_x, \ddot{\theta}_y \in \mathcal{L}_\infty \Rightarrow \ddot{e}_x, \ddot{e}_y, \ddot{e}_z, \ddot{e}_l \in \mathcal{L}_\infty. \quad (27)$$

On the basis of (24)–(26), one has that

$$\begin{aligned} & k_{dx} \int_0^t \dot{e}_x^2 d\tau + k_{dy} \int_0^t \dot{e}_y^2 d\tau + k_{dz} \int_0^t \dot{e}_z^2 d\tau + k_{dl} \int_0^t \dot{e}_l^2 d\tau \\ & + \frac{1}{2} d_p l^2 \int_0^t \left(\dot{\theta}_x^2 C_y^2 + \dot{\theta}_y^2 \right) d\tau \\ & \leq -V_2(t) + V_2(0) + \left(\frac{m^2}{d_p} + m \right) \int_0^t \ddot{x}_d^2 d\tau + (d_p + m) \int_0^t \dot{x}_d^2 d\tau \\ & + \left(\frac{m^2}{2d_p} + \frac{m}{2} \right) \int_0^t \ddot{y}_d^2 d\tau + \frac{d_p + m}{2} \int_0^t \dot{y}_d^2 d\tau + \left(\frac{m^2}{d_p} + m \right) \int_0^t \ddot{z}_d^2 d\tau \\ & + (d_p + m) \int_0^t \dot{z}_d^2 d\tau + 2mg\bar{l} \ll +\infty \end{aligned}$$

which leads to

$$\dot{e}_x(t), \dot{e}_y(t), \dot{e}_z(t), \dot{e}_l(t), \dot{\theta}_x(t), \dot{\theta}_y(t) \in \mathcal{L}_2. \quad (28)$$

Collecting the results in (26)–(28), and invoking Barbalat's Lemma, the following results are obtained as

$$\begin{aligned} & \lim_{t \rightarrow \infty} \dot{e}_x(t) = 0, \lim_{t \rightarrow \infty} \dot{e}_y(t) = 0, \lim_{t \rightarrow \infty} \dot{e}_z(t) = 0 \\ & \lim_{t \rightarrow \infty} \dot{e}_l(t) = 0, \lim_{t \rightarrow \infty} \dot{\theta}_x(t) = 0, \lim_{t \rightarrow \infty} \dot{\theta}_y(t) = 0. \end{aligned} \quad (29)$$

Subsequently, according to (12) and (29), one can derive that

$$\lim_{t \rightarrow \infty} \dot{x}(t) = \lim_{t \rightarrow \infty} \dot{y}(t) = \lim_{t \rightarrow \infty} \dot{z}(t) = \lim_{t \rightarrow \infty} \dot{l}(t) = 0. \quad (30)$$

Thus, it can be concluded that

$$\lim_{t \rightarrow \infty} f_{rx} = \lim_{t \rightarrow \infty} f_{ry} = \lim_{t \rightarrow \infty} f_{rz} = \lim_{t \rightarrow \infty} f_{rl} = \lim_{t \rightarrow \infty} f_{r\theta_x} = \lim_{t \rightarrow \infty} f_{r\theta_y} = 0 \quad (31)$$

$$\lim_{t \rightarrow \infty} \phi_x = \lim_{t \rightarrow \infty} \phi_y = \lim_{t \rightarrow \infty} \phi_z = \lim_{t \rightarrow \infty} \phi_l = \mathbf{0}_{2 \times 1}. \quad (32)$$

In the following analysis, the convergence of $e_x(t)$, $e_y(t)$, $e_z(t)$, $e_l(t)$, $\theta_x(t)$, and $\theta_y(t)$ will be further analyzed. Rewrite (5) and (6) as

$$\begin{aligned} ml\ddot{\theta}_x C_y &= -m\ddot{x}C_x - m\ddot{z}S_x - 2ml\dot{\theta}_x C_y + 2ml\dot{\theta}_x \dot{\theta}_y S_y \\ &- mgS_x + \frac{f_{r\theta_x}}{lC_y} \end{aligned} \quad (33)$$

$$\begin{aligned} ml\ddot{\theta}_y &= m\ddot{x}S_x S_y - m\ddot{y}C_y - m\ddot{z}C_x S_y - 2ml\dot{\theta}_y \\ &- ml\dot{\theta}_x^2 C_y S_y - mgC_x S_y + \frac{f_{r\theta_y}}{l}. \end{aligned} \quad (34)$$

Subsequently, substituting (16), (33) and (34) to (1)–(4) leads to

$$\begin{aligned} & (M + mS_x^2 C_y^2) \ddot{x} + mS_x C_y S_y \ddot{y} - mS_x C_x C_y^2 \ddot{z} + m\ddot{l} S_x C_y \\ & = \delta_x + \varepsilon_x \end{aligned} \quad (35)$$

$$\begin{aligned} & mS_x C_y S_y \ddot{x} + (M + mS_y^2) \ddot{y} - mC_x C_y S_y \ddot{z} + m\ddot{l} S_y \\ & = \delta_y + \varepsilon_y \end{aligned} \quad (36)$$

$$\begin{aligned} & -mC_x S_x C_y^2 \ddot{x} - mC_x C_y S_y \ddot{y} + (M + mC_x^2 C_y^2) \ddot{z} - m\ddot{l} C_x C_y \\ & = \delta_z + \varepsilon_z \end{aligned} \quad (37)$$

$$mS_x C_y \ddot{x} + mS_y \ddot{y} - m\ddot{z} C_x C_y + m\ddot{l} = \delta_l + \varepsilon_l \quad (38)$$

where

$$\begin{aligned} \delta_x &= -k_{dx} \dot{e}_x + \phi_x^\top \hat{\omega}_x + (M + m) \ddot{x}_d + mS_x C_y \ddot{l}_d \\ &+ m \left(\dot{\theta}_x C_x C_y - \dot{\theta}_y S_x S_y \right) \dot{l}_d + f_{rx} - \frac{C_x f_{r\theta_x}}{lC_y} \\ &- \frac{S_x S_y f_{r\theta_y}}{l} + ml\dot{\theta}_x^2 S_x C_y^3 + ml\dot{\theta}_y^2 S_x C_y \end{aligned}$$

$$\begin{aligned} \delta_y &= -k_{dy} \dot{e}_y + \phi_y^\top \hat{\omega}_y + (M + m) \ddot{y}_d + mS_y \ddot{l}_d + m\dot{\theta}_y C_y \dot{l}_d \\ &+ f_{ry} - \frac{C_y f_{r\theta_y}}{l} + ml\dot{\theta}_x^2 C_y^2 S_y + ml\dot{\theta}_y^2 S_y \end{aligned}$$

$$\begin{aligned} \delta_z &= -k_{dz} \dot{e}_z + \phi_z^\top \hat{\omega}_z + (M + m) \ddot{z}_d - mC_x C_y \ddot{l}_d \\ &+ m \left(\dot{\theta}_x C_y S_x + \dot{\theta}_y C_x S_y \right) \dot{l}_d + f_{rz} - \frac{S_x f_{r\theta_x}}{lC_y} \\ &- \frac{C_x S_y f_{r\theta_y}}{l} - ml\dot{\theta}_x^2 C_x C_y^3 - ml\dot{\theta}_y^2 C_x C_y \end{aligned}$$

$$\begin{aligned} \delta_l &= -k_{dl} \dot{e}_l + \phi_l^\top \hat{\omega}_l + m\ddot{l}_d + mS_x C_y \ddot{x}_d + mS_y \ddot{y}_d \\ &- mC_x C_y \ddot{z}_d + f_l + ml\dot{\theta}_x^2 C_y^2 + ml\dot{\theta}_y^2 \end{aligned}$$

$$\varepsilon_x = -k_{px} e_x + mgC_x S_x C_y^2, \varepsilon_y = -k_{py} e_y + mgC_x C_y S_y$$

$$\varepsilon_z = -k_{pz} e_z + mg(1 - C_x^2 C_y^2), \varepsilon_l = -k_{pl} e_l - mg(1 - C_x C_y).$$

On the basis of the analysis in (26)–(32), it is straightforward to conclude that

$$\lim_{t \rightarrow \infty} \delta_x = \lim_{t \rightarrow \infty} \delta_y = \lim_{t \rightarrow \infty} \delta_z = \lim_{t \rightarrow \infty} \delta_l = 0, \dot{e}_x, \dot{e}_y, \dot{e}_z, \dot{e}_l \in \mathcal{L}_\infty. \quad (39)$$

Moreover, by substituting (38) into (35)–(37) and making some transformation, one has

$$\begin{aligned} \ddot{x} &= \frac{-(\delta_l + \varepsilon_l) S_x C_y + \delta_x + \varepsilon_x}{M} = \mu_x + \nu_x \\ \ddot{y} &= \frac{-(\delta_l + \varepsilon_l) S_y + \delta_y + \varepsilon_y}{M} = \mu_y + \nu_y \\ \ddot{z} &= \frac{-(\delta_l + \varepsilon_l) C_x C_y + \delta_z + \varepsilon_z}{M} = \mu_z + \nu_z \\ \ddot{l} &= \frac{\delta_l + \varepsilon_l}{m} - S_x C_y \ddot{x} - S_y \ddot{y} + C_x C_y \ddot{z} = \mu_l + \nu_l \end{aligned}$$

where

$$\mu_x = \frac{-\delta_l S_x C_y + \delta_x}{M}, \nu_x = \frac{-\varepsilon_l S_x C_y + \varepsilon_x}{M}, \mu_y = \frac{-\delta_l S_y + \delta_y}{M}$$

$$\nu_y = \frac{-\varepsilon_l S_y + \varepsilon_y}{M}, \mu_z = \frac{-\delta_l C_x C_y + \delta_z}{M}, \nu_z = \frac{-\varepsilon_l C_x C_y + \varepsilon_z}{M}$$

$$\mu_l = \frac{\delta_l}{m} - S_x C_y \mu_x - S_y \mu_y + C_x C_y \mu_z$$

$$\nu_l = \frac{\varepsilon_l}{m} - S_x C_y \nu_x - S_y \nu_y + C_x C_y \nu_z.$$

According to (39), it is obvious that

$$\lim_{t \rightarrow \infty} \mu_x = \lim_{t \rightarrow \infty} \mu_y = \lim_{t \rightarrow \infty} \mu_z = \lim_{t \rightarrow \infty} \mu_l = 0, \dot{\nu}_x, \dot{\nu}_y, \dot{\nu}_z, \dot{\nu}_l \in \mathcal{L}_{\infty}. \quad (40)$$

Based on the extended Barbalat's Lemma, gathering the results of (30) and (40) leads to

$$\lim_{t \rightarrow \infty} \ddot{x} = \lim_{t \rightarrow \infty} \ddot{y} = \lim_{t \rightarrow \infty} \ddot{z} = \lim_{t \rightarrow \infty} \ddot{l} = 0. \quad (41)$$

Utilizing the similar analysis method, $\ddot{\theta}_x$ and $\ddot{\theta}_y$ are rewritten as

$$\ddot{\theta}_x = \mu_{\theta_x} + \nu_{\theta_x}, \ddot{\theta}_y = \mu_{\theta_y} + \nu_{\theta_y} \quad (42)$$

where

$$\begin{aligned} \mu_{\theta_x} &= -\frac{\ddot{x}C_x}{lC_y} - \frac{\ddot{z}S_x}{lC_y} - \frac{2\dot{l}\dot{\theta}_x}{l} + \frac{2\dot{\theta}_x\dot{\theta}_y S_y}{C_y} + \frac{f_{r\theta_x}}{ml^2 C_y^2} \\ \mu_{\theta_y} &= \frac{\ddot{x}S_x S_y}{l} - \frac{\ddot{y}C_y}{l} - \frac{\ddot{z}C_x S_y}{l} - \frac{2\dot{l}\dot{\theta}_y}{l} - \frac{l\dot{\theta}_x^2 C_y S_y}{l} + \frac{f_{r\theta_y}}{ml^2} \\ \nu_{\theta_x} &= -\frac{gS_x}{lC_y}, \nu_{\theta_y} = -\frac{gC_x S_y}{l}. \end{aligned}$$

Combining with the results in (26)–(32) and (41), one can derive the following conclusion:

$$\lim_{t \rightarrow \infty} \mu_{\theta_x} = \lim_{t \rightarrow \infty} \mu_{\theta_y} = 0, \dot{\nu}_{\theta_x}, \dot{\nu}_{\theta_y} \in \mathcal{L}_{\infty}. \quad (43)$$

Again, utilizing the extended Barbalat's Lemma and the consequence of (30) and (43), the following conclusion can be drawn:

$$\lim_{t \rightarrow \infty} \ddot{\theta}_x = \lim_{t \rightarrow \infty} \ddot{\theta}_y = 0. \quad (44)$$

Furthermore, exploiting (42) and (44), one has

$$\lim_{t \rightarrow \infty} \nu_{\theta_x} = \lim_{t \rightarrow \infty} \nu_{\theta_y} = 0 \Rightarrow \lim_{t \rightarrow \infty} \theta_x = \lim_{t \rightarrow \infty} \theta_y = 0. \quad (45)$$

Next, applying (31), (41) and (45) to (1)–(4) produces

$$\lim_{t \rightarrow \infty} \mathbf{u} = [0, 0, (M+m)g, -mg]^T. \quad (46)$$

Finally, with the conclusion in (12), (29), (32), and (46), according to (16), it is further indicated that

$$\lim_{t \rightarrow \infty} e_x = \lim_{t \rightarrow \infty} e_y = \lim_{t \rightarrow \infty} e_z = \lim_{t \rightarrow \infty} e_l = 0. \quad (47)$$

As a result, from (29), (45), and (47), Theorem 1 is proved. ■

Remark 3: As shown in model (1)–(6), the dynamics of the cable length are coupled with quadrotor motion and payload swing seriously. Thus, although the cable adjustment mechanism greatly improves the flexibility and the adaptability of the system, it also brings strong nonlinearity and complex dynamic coupling due to the variable-length cable dynamics, which leads to great difficulties in precise control and the corresponding theoretical analysis. Due to the strong nonlinearity, high DOFs and complex dynamic coupling, it is difficult to design control schemes for such underactuated systems based on input–output feedback linearization and guarantee the convergence of the payload swing angles, which is the indispensable condition to ensure accurate payload landing. Thus, the energy-based controller design method is applied in this article, which realizes

trajectory tracking and payload swing suppression, simultaneously. To the best of authors' knowledge, this article presents the first tracking control law design for the variable-length-cable-suspended aerial transportation system with detailed stability analysis, which aims at overcoming the difficulties in stability analysis caused by the variable-length cable dynamics and the unknown resistance coefficient in the actual flight.

Remark 4: It is worth noting that although the persistent-excitation condition [44] is not satisfied when estimating the unknown resistance coefficient, it does not affect the conclusion that the tracking error and payload swing angles converge to zero. However, under the adaptive control framework, the estimation of the unknown payload mass is not available, which is still a problem that needs to be solved in future work.

Theorem 2: Based on the control scheme (16), (19) and update law (17), the tracking error of the closed-loop system converge to zero, i.e.,

$$\begin{aligned} &\lim_{t \rightarrow \infty} [\mathbf{e}_\alpha^\top, \Theta^\top, \dot{\mathbf{e}}_\alpha^\top, \dot{\Theta}^\top, \mathbf{e}_R^\top, \mathbf{e}_\Omega^\top]^\top \\ &= [\mathbf{0}_{4 \times 1}^\top, \mathbf{0}_{2 \times 1}^\top, \mathbf{0}_{4 \times 1}^\top, \mathbf{0}_{2 \times 1}^\top, \mathbf{0}_{3 \times 1}^\top, \mathbf{0}_{3 \times 1}^\top]^\top. \end{aligned}$$

Proof: In Theorem 1, \mathbf{u}_Δ is temporarily neglected, while it is taken into account here. Define the generalized outerloop error vector as $\mathbf{e}_q = [\mathbf{e}^\top, \dot{\mathbf{e}}^\top]^\top$, and λ_p, λ_d as the maximum eigenvalues for control gains K_p, K_d . Based on the results in (26) and (11), one can find a constant $C \in \mathbb{R}_+$ satisfying $\|M\Xi_d\| + \|m\Psi_d\| + \|\hat{\Phi}_\omega\| \leq C$. Thus, the virtual control input (16) can be scaled to

$$\begin{aligned} \|\mathbf{u}\| &\leq \|K_p \mathbf{e}_\alpha\| + \|K_d \dot{\mathbf{e}}_\alpha\| + \|M\Xi_d\| + \|m\Psi_d\| + \|\hat{\Phi}_\omega\| \\ &\leq \sqrt{2} \max(\lambda_p, \lambda_d) \|\mathbf{e}_q\| + C \\ &= \sqrt{2} \max(\lambda_p, \lambda_d) \left(\frac{C}{\sqrt{2} \max(\lambda_p, \lambda_d)} + \|\mathbf{e}_q\| \right). \end{aligned}$$

By setting $\varepsilon = \sqrt{2} \max(\lambda_p, \lambda_d)$, $\epsilon = \frac{C}{\sqrt{2} \max(\lambda_p, \lambda_d)} + \|\mathbf{e}_q\|$, and choosing the class- \mathcal{K} function $\iota(\mathbf{e}_R) = \varepsilon \|\Pi_{01} M_c^{-1} F\| \|\mathbf{e}_R\|$, $c_\Delta = \epsilon$, where $\Pi_{01} = [0_{6 \times 6}, I_{6 \times 6}]^\top$. Therefore, the growth restriction condition $\|\Pi_{01} M_c^{-1} [\mathbf{u}_\Delta^\top, 0, 0]^\top\| \leq \iota(\mathbf{e}_R) \|\mathbf{e}_q\|$, for $\|\mathbf{e}_q\| \geq c_\Delta$ can be further proven similar to [33], [42], [43]. Finally, combining with Theorem 1, Theorem 2 can be proved. ■

IV. SIMULATION AND EXPERIMENTAL IMPLEMENTATION

In this section, some groups of simulation and experimental tests are implemented to verify the feasibility of the proposed tracking controller.

A. Numerical Simulation and Analysis

The dynamic model is established in the MATLAB/Simulink environment, and the parameters of the aerial transportation system are chosen as $M = 2.0 \text{ kg}$, $m = 0.4 \text{ kg}$, $g = 9.8 \text{ m/s}^2$. The control gains are selected as $K_p = \text{diag}([5.0, 5.0, 8.0, 10.0])$, $K_d = \text{diag}([6.0, 6.0, 9.0, 6.0])$, $\Gamma_x = \Gamma_y = \Gamma_z = \Gamma_l = \text{diag}([1.0, 1.0])$. Specifically, the desired trajectories satisfy Property

2 are selected as

$$\begin{aligned}x_d(t) &= \frac{p_{dx} + x_0}{2} + \frac{1}{2\varrho_x} \ln \left[\frac{\cosh(\sigma_x t - \zeta_x)}{\cosh(\sigma_x t - \zeta_x - (p_{dx} - x_0) \varrho_x)} \right] \\y_d(t) &= \frac{p_{dy} + y_0}{2} + \frac{1}{2\varrho_y} \ln \left[\frac{\cosh(\sigma_y t - \zeta_y)}{\cosh(\sigma_y t - \zeta_y - (p_{dy} - y_0) \varrho_y)} \right] \\z_d(t) &= \frac{p_{dz} + z_0}{2} + \frac{1}{2\varrho_z} \ln \left[\frac{\cosh(\sigma_z t - \zeta_z - |p_{dz} - z_0| \varrho_z)}{\cosh(\sigma_z t - \zeta_z)} \right] \\l_d(t) &= \frac{p_{dl} + l_0}{2} + \frac{1}{2\varrho_l} \ln \left[\frac{\cosh(\sigma_l t - \zeta_l)}{\cosh(\sigma_l t - \zeta_l - (p_{dl} - l_0) \varrho_l)} \right]\end{aligned}$$

where ζ_k is the positive undetermined constant, $\varrho_k = 2\bar{a}_k/\bar{v}_k^2$ and $\sigma_k = 2\bar{a}_k/\bar{v}_k$, for $k = x, y, z, l$. Two groups of simulation results are presented to verify the controller's performance, which greatly testify the superiority to cope with different resistance coefficient parameters and the robustness to deal with the external perturbations.

1) Simulation I: Different Resistance Coefficient Test: To verify the ability of the proposed control method and the update law when dealing with parameter uncertainties, three groups of simulations are implemented by setting different unknown resistance coefficient parameters. The three groups of resistance coefficient parameters are set as

- 1) $D_\alpha = \text{diag}([0.4, 0.4, 0.4, 0.3])$, $d_p = 0.2$;
- 2) $D_\alpha = \text{diag}([0.8, 0.8, 1.5, 0.6])$, $d_p = 0.4$;
- 3) $D_\alpha = \text{diag}([1.8, 1.8, 1.2, 0.8])$, $d_p = 0.4$.

Besides, the parameters of the trajectories are selected as $\bar{v}_x = 0.6$, $\bar{v}_y = 0.70$, $\bar{v}_z = 0.6$, $\bar{v}_l = 0.3$, $\bar{a}_x = 0.55$, $\bar{a}_y = 0.65$, $\bar{a}_z = 0.55$, $\bar{a}_l = 0.25$, $\zeta_x = \zeta_y = \zeta_z = \zeta_l = 2.0$. The initial and the preset final quadrotor position and cable length vectors are set as $p_0 = [0.0, 0.0, 4.0, 0.7]^\top$ m and $p_d = [2.0, 3.0, 2.0, 1.8]^\top$ m, respectively. The obtained simulation results are given in Fig. 3, from which one can find that even under different resistance coefficients, the quadrotor, and the cable length can eventually track the desired trajectory within a small payload swing angle range. Besides, as shown in Fig. 3(c), the adaptive update law can effectively deal with different resistance coefficients, and the estimations finally converge to constants.

2) Simulation II: Robustness Test: In this group, the robustness of the designed control scheme is investigated by adding perturbations on the quadrotor and the payload. The parameters of the trajectories are selected as $\bar{v}_x = 0.48$, $\bar{v}_y = 0.7$, $\bar{v}_z = 0.48$, $\bar{v}_l = 0.19$, $\bar{a}_x = 0.45$, $\bar{a}_y = 0.65$, $\bar{a}_z = 0.45$, $\bar{a}_l = 0.15$, $\zeta_x = \zeta_y = \zeta_z = \zeta_l = 5.0$, and the initial and preset final quadrotor position and cable length vectors are set as $p_0 = [0.0, 0.0, 30.0, 1.0]^\top$ m and $p_d = [20.0, 30.0, 10.0, 9.0]^\top$ m. The resistance coefficient parameters is set the same as the first group of Simulation I. Impulse perturbations are added on the x -axis and y -axis of the quadrotor with the amplitude of 7 N and -5 N at 10 s and 20 s, and on the payload with the amplitude of 8 N and -5 N at 30 s and 40 s during flight. The simulation curves are presented in Fig. 4. Due to the influence of the external disturbances, the shift in quadrotor position reach $e_x = 0.3512$ m and $e_y = 0.3908$ m at 10 s and 20 s correspondingly, and the payload produces large swing angles. In spite of this, the proposed method can deal with the disturbance rapidly, and anti the

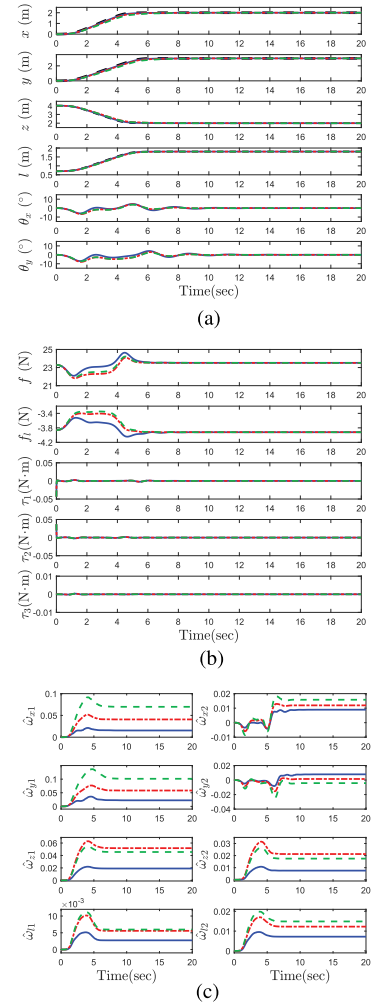


Fig. 3. Results for Simulation I. (Blue solid lines: Results for Group 1. Red dotted lines: Results for Group 2. Green dotted lines: Results for Group 3. Black dotted lines: Desired trajectories.). (a) Quadrotor position, cable length, and payload swing angles. (b) Control inputs. (c) Parameter estimates.

payload swing. Besides, even the disturbance is applied to the payload, the oscillation can be effectively suppressed.

B. Experimental Platform

Fig. 5 presents the self-built experimental platform, which is consisted of variable-length-cable-suspended aerial transportation system, Qualisys motion capture system, ground station, and router. The utilized F450 quadrotor is equipped with 2216-KV950 brushless motors and 30A electronic speed control. The cable adjustment mechanism is composed of a Dynamixel MX-64 actuator, a 3-D-printed quadrotor-actuator connector, and a 3-D-printed spool. The flight control unit of the quadrotor is PixHawk 2.4.8, whose built-in IMU is utilized to measure the attitude of the quadrotor. An onboard computing unit Raspberry Pi 4B with high-cost performance and light quality is mounted on the quadrotor to send control instructions to PixHawk and Dynamixel through Micro Air Vehicle Link (MavLink) and RS-485 communication protocol. The Qualisys motion capture system consisting of eight cameras and a computer, is utilized to

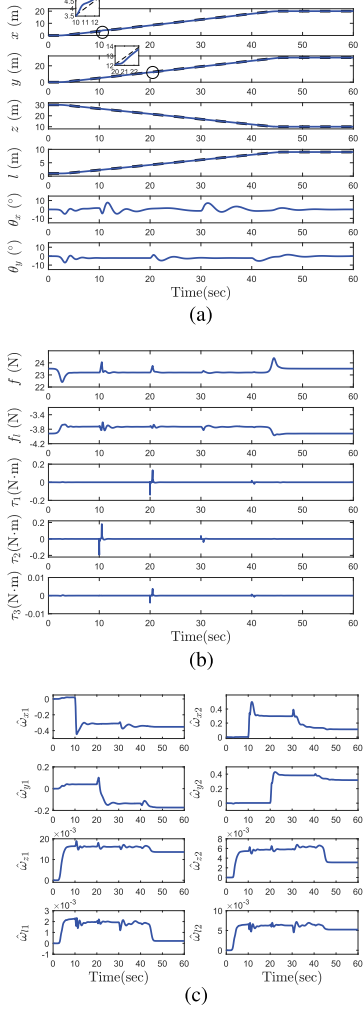


Fig. 4. Results for Simulation II. (Blue solid lines: Results by the proposed method. Black dotted lines: Desired trajectories.). (a) Quadrotor position, cable length, and payload swing angles. (b) Control inputs. (c) Parameter estimates.

identify markers on the quadrotor and payload so as to calculate the quadrotor's translational motion, cable length, and payload swing angles. The ground station sends the desired trajectories of the quadrotor and the cable length to the onboard computing unit via WiFi signals broadcast by the router. The whole system runs with the support of robot operating system (ROS) in Linux environment. As presented in Fig. 2, based on the trajectory tracking controller (16) and the attitude tracking control approach (19), the control input for the aerial transportation system can be obtained. The actuating force generated by the cable adjustment mechanism f_l is sent to Dynamixel, and the quadrotor thrust f and torque τ are sent to PixHawk. Based on the basic PX4 code, the desired quadrotor thrust is transmitted to throttle to $0 \sim 1$ by $k_f \cdot (f - G_s) + u_h$, where $u_h = 0.56$ is the hover throttle, $k_f = 0.2 \cdot \frac{1}{G_s}$ is the proportionality coefficient, $G_s = (M + m)g$. Besides, the torque is transmitted to the desired angular velocity with the integral approximation as $k_o \cdot \frac{1}{\text{fre}} \cdot \tau$, where fre = 100Hz is the frequency of the inner loop, $k_o = 250$ is a constant gain.

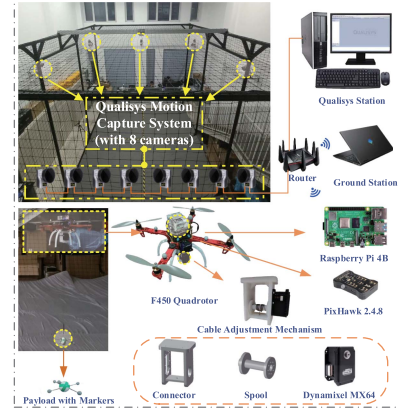


Fig. 5. Experimental platform.

The physical parameters of the experimental platform are given as $M = 1.74 \text{ kg}$, $g = 9.8 \text{ m/s}^2$. To achieve satisfactory trajectory tracking and the antiswing control objective, we repeat a couple of times for the experiment to tune the control parameters with experience. The control gains are selected as $K_p = \text{diag}([4.0, 4.0, 8.0, 18.0])$, $K_d = \text{diag}([6.5, 6.5, 14.0, 8.0])$, $\Gamma_x = \Gamma_y = \Gamma_z = \Gamma_l = \text{diag}([1.0, 1.0])$. In the following section, a basic performance test and a function demonstration test are conducted based on the experimental platform. The video of the experiment is available in <https://youtu.be/yzVDjaOVj04>.

C. Experimental Results

1) Experiment I: Basic Performance Test: This part presents the basic performance verification for the tracking controller. The ultimate goal is to drive the quadrotor to the desired position and adjust the cable to the desired length. In this part, the payload mass is $m = 0.103 \text{ kg}$.

Test 1: The initial and the preset final quadrotor position and cable length vector of the quadrotor and the cable are set as $\mathbf{p}_0 = [0.0, 0.0, 1.8, 0.7]^\top \text{m}$ and $\mathbf{p}_d = [1.8, 2.2, 1.2, 0.9]^\top \text{m}$, respectively. The trajectories are selected the same as the simulation part, and the parameters are set as $\bar{v}_x = 0.65$, $\bar{v}_y = 0.90$, $\bar{v}_z = 0.24$, $\bar{v}_l = 0.17$, $\bar{a}_x = 0.60$, $\bar{a}_y = 0.85$, $\bar{a}_z = 0.22$, $\bar{a}_l = 0.08$, $\zeta_x = \zeta_y = \zeta_z = \zeta_l = 1.2$. Since there exists no literatures about trajectory tracking control methods for the discussed aerial transportation system with variable-length cable, the PD controller $\mathbf{F}_{PD} = -K_{p_{pd}} \mathbf{e}_p - K_{d_{pd}} \dot{\mathbf{e}}_p + [0, 0, (M + m)g, -mg]^\top$ and the linear quadratic regulator (LQR) controller $\mathbf{F}_{LQR} = -K_{p_{lqr}} \mathbf{e}_p - K_{d_{lqr}} \dot{\mathbf{e}}_p - K_{\theta_{lqr}} [\Theta^\top, 0, 0]^\top - K_{\dot{\theta}_{lqr}} [\dot{\Theta}^\top, 0, 0]^\top + [0, 0, (M + m)g, -mg]^\top$ are chosen as comparative control schemes, where $\mathbf{e}_p = [e_{px}, e_{py}, e_{pz}, e_{pl}]^\top = [x - p_{dx}, y - p_{dy}, z - p_{dz}, l - p_{dl}]^\top$, and the control gains are chosen as

$$K_{p_{pd}} = \text{diag}([4.0, 4.0, 8.0, 15.0])$$

$$K_{d_{pd}} = \text{diag}([6.5, 6.5, 14.0, 6.0])$$

$$K_{\theta_{lqr}} = \text{diag}([-0.7674, -0.7674, 0, 0])$$

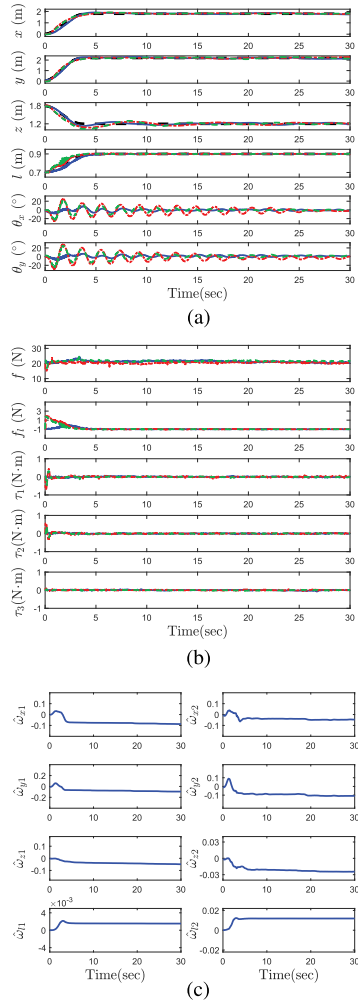


Fig. 6. Results for Exp I-T1. (Blue solid lines: Results by the proposed method. Red dotted lines: Results by the PD method. Green dotted lines: Results by the LQR method. Black dotted lines: Desired trajectories.). (a) Quadrotor position, cable length and payload swing angles. (b) Control inputs. (c) Parameter estimates.

$$K_{\dot{\theta}_{lqr}} = \text{diag}([-0.0995, -0.0995, 0, 0])$$

$$K_{p_{lqr}} = \begin{bmatrix} 4.0000 & 0 & 0 & 0 \\ 0 & 4.0000 & 0 & 0 \\ 0 & 0 & 7.7431 & -0.3875 \\ 0 & 0 & 0.2122 & 14.1368 \end{bmatrix}$$

$$K_{d_{lqr}} = \begin{bmatrix} 6.2246 & 0 & 0 & 0 \\ 0 & 6.2246 & 0 & 0 \\ 0 & 0 & 12.1844 & -0.3509 \\ 0 & 0 & 0.2279 & 5.7357 \end{bmatrix}.$$

Fig. 6 provides the results of the proposed controller and the comparative ones, from which one can find that all methods could drive the variable-length-cable-suspend aerial transportation system to the target quadrotor position and cable length within 5 s. The indexes on the maximum and root mean square (RMS) values of payload swing angles and trajectory tracking errors are presented in Tables II and III, respectively, based on which one can find that the swing angles' maximum and RMS values of the proposed method are obviously smaller

TABLE II
QUANTITATIVE DATA OF PAYLOAD SWING ANGLES

ExpI-T1	max		RMS	
	θ_x (°)	θ_y (°)	θ_x (°)	θ_y (°)
Pro. controller	8.5652	8.4102	2.4279	2.3591
LQR controller	23.6697	25.2789	5.8479	6.4155
PD controller	27.5882	30.3067	8.4733	8.7156

TABLE III
QUANTITATIVE DATA OF TRACKING ERRORS

ExpI-T1	e_x (m)	e_y (m)	e_z (m)	e_l (m)
max	0.2036	0.1771	0.0810	0.0411
RMS	0.0586	0.0523	0.0291	0.0077

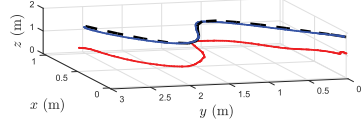


Fig. 7. Trajectories for Exp I-T2. (Black dotted line: Reference quadrotor trajectory. Blue solid lines: Actual quadrotor trajectory. Red solid lines: Actual payload trajectory.)

than the comparative methods. Besides, the tracking errors are kept within a small range. Moreover, all control schemes can suppress the payload swing, while the proposed tracking control scheme exhibits better antiswing performance. As presented in Fig. 6(c), it is worth noting that all resistance coefficient parameters converge under the proposed update law. Although the estimations of the second element of vector $\omega_x, \omega_y, \omega_z, \omega_l$ converge to different values, the tracking error still converges to zero due to the adaption law.

Test 2: To further verify the performance of the designed controller, an elaborately designed trajectory with different shape is selected as the desired trajectory in Fig. 7. The trajectory is generated by the classical minimum snap trajectory generation method [35], whose waypoints in $x-y$ plane are selected as $[0, 0]^T$ m, $[1, 1]^T$ m, $[0.5, 2]^T$ m, $[1, 2.5]^T$ m. The initial and the preset final quadrotor position and cable length vector of the quadrotor and the cable are set as $p_0 = [0.0, 0.0, 1.8, 0.7]^T$ m and $p_d = [1.0, 2.5, 1.2, 0.9]^T$ m, respectively. The quadrotor height trajectory and cable length trajectory are selected the same as the simulation part, whose parameters are set as $\bar{v}_z = 0.24$, $\bar{v}_l = 0.17$, $\bar{a}_z = 0.22$, $\bar{a}_l = 0.08$, $\zeta_z = \zeta_l = 2.0$. Based on the experimental results in Figs. 7 and 8, one can find that even the desired trajectory has a large radian, the tracking error and the payload swing angles are kept within a small range. Besides, the estimations of the resistance coefficients constantly updated during the flight, and finally converge to constants.

2) Experiment II: Function Demonstration Test: In this part, the performance of the proposed control strategy is further verified for the scenario to land the payload onto the mobile platform. To simulate this scenario, the payload is connected with an electromagnetic switch, as shown in Fig. 9, which is made up of an electromagnet, a relay module, a Raspberry Pi Zero computing unit, and a lithium battery. The Raspberry Pi

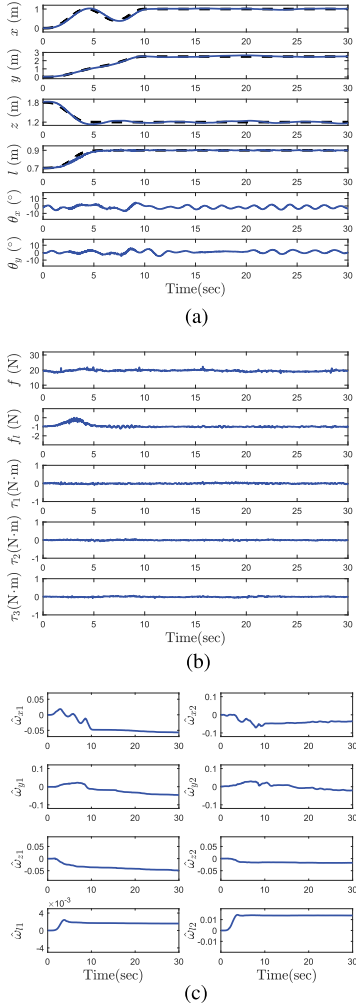


Fig. 8. Results for Exp I-T2. (Blue solid lines: Results by the proposed method. Black dotted lines: Desired trajectories.). (a) Quadrotor position, cable length and payload swing angles. (b) Control inputs. (c) Parameter estimates.

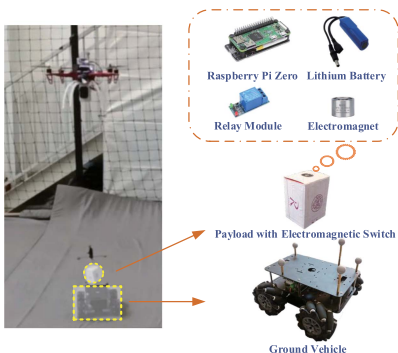


Fig. 9. Electromagnetic switch to release the payload for Exp II.

Zero sends control signals to the relay module, which acts as a low-level triggered circuit switch, while the lithium battery powers the electromagnet. During the payload transportation process, the relay module keeps closing and the electromagnet remains energized. The mobile platform equipped with markers is identified by the motion capture system to obtain its position

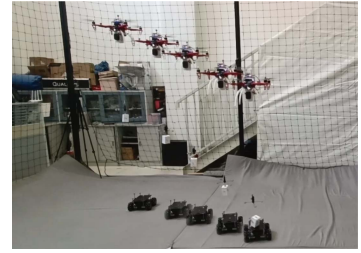


Fig. 10. Snap of the landing process.

Algorithm 1: Payload Release Trigger.

Input: Mobile platform position $\xi_m = [x_m, y_m, z_m]^\top$; Mobile platform side length s_{mx}, s_{my} ; Payload position $\xi_p = [x_p, y_p, z_p]^\top$; Release distance d_r .
Output: Payload release signal r_s .

```

1 while True do
2   Update  $\xi_m, \xi_p$ ;
3   if  $0 < z_p - z_m \leq d_r$  and  $|x_p - x_m| < \frac{1}{2}s_{mx}$  and
    $|y_p - y_m| < \frac{1}{2}s_{my}$  then
4     Send signal  $r_s$ ;
5     Break;
6   end
7 end
```

and velocity, which is mainly composed of four direct current (dc) motors, a bottom control board, and a Raspberry Pi 4B upper control unit. The bottom control board directly controls the four dc motors and communicates with the upper control unit. Under the ROS framework, the mobile platform is controlled by speed signals. During the experiment, the program judges whether the payload meets the landing condition. For successful payload landing, the relative vertical distance between the payload and the mobile platform needs to be small enough. In addition, due to the limited size of the mobile platform, the payload should be kept within the boundary of the mobile platform. When the abovementioned landing condition meets, the program will send the release signal. The corresponding pseudocode is given in Algorithm 1. When Raspberry Pi Zero received the release signal from the ground station, the level of the general-purpose input/output (GPIO) port connected to the relay module's trigger port changes, so that the relay module opens and the payload is released. The snap of the payload landing process is given in Fig. 10. All parts of the system operate under ROS.

In this group of experiment, the payload is changed from a ball to a cuboid while the mass of the payload is $m = 0.168$ kg, which is increased by 63% compared with Experiment I. The parameters of the trajectory are selected as $\bar{v}_x = 0.22$, $\bar{v}_y = 0.35$, $\bar{v}_z = 0.20$, $\bar{v}_l = 0.17$, $\bar{a}_x = 0.15$, $\bar{a}_y = 0.28$, $\bar{a}_z = 0.15$, $\bar{a}_l = 0.08$, $\zeta_x = \zeta_y = \zeta_z = \zeta_l = 2.0$, $p_0 = [0.0, 0.0, 1.8, 0.7]^\top$ m, and $p_d = [1.8, 3.0, 1.2, 0.9]^\top$ m. Without loss of generality, the trajectory of the mobile platform is set the same as the quadrotor's trajectory in x -axis and y -axis for the demonstration test. The height of the quadrotor and the length of the cable first achieve the desired value, then at $t = 5$ s, the

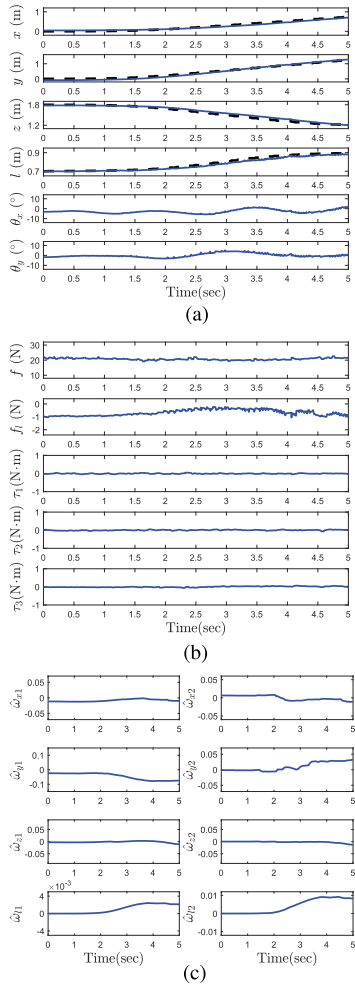


Fig. 11. Results for Exp II. (Blue solid lines: Results by the proposed method. Black dotted lines: Desired trajectories.). (a) Quadrotor position, cable length, and payload swing angles. (b) Control inputs. (c) Parameter estimates.

payload release condition is satisfied and the release signal is sent. The experiment curves are given in Fig. 11, from which one can see that although the shape and mass of the payload have changed, the proposed control law can still ensure the smooth transportation of the payload, which has good tracking performance and antiswing ability. Besides, Fig. 10 shows that the proposed control scheme can drive the payload landing onto the mobile platform precisely, which is the prerequisite for the landing mission.

Remark 5: To land the payload onto a mobile platform, the following aspects should be guaranteed: 1) landing trajectory generation for both the mobile platform and the quadrotor; 2) tracking for the generated trajectory and suppression of the payload swing during transportation and landing. In fact, although the motion information of the mobile platform could be obtained, the safe landing of the payload cannot be guaranteed, because the aerial transportation system is underactuated, that is, the motion of the payload cannot be directly controlled. For the problem of payload landing onto the mobile platform, this article tries from two aspects: 1) When the payload landing position

range is determined, i.e., the initial and target positions are determined, the trajectories of the quadrotor and the mobile platform that meet specific constraints are proposed, and the motion in the x and y directions are consistent. 2) The trajectory tracking control strategy for the aerial transportation system is designed. This cooperation way between the quadrotor and the mobile platform will help improve the success rate of payload landing. In the future, we will construct outdoor experimental platform, which will transmit information based on WiFi, ZigBee, etc. Besides, we will install such sensors as cameras and lidars onto the aerial transportation system to obtain the motion information of the mobile platform in real time, so as to continuously provide the feedback signal and improve the robustness of the system. With the help of sensing devices, it is also expected to provide a replanning solution when the target is not synchronized.

V. CONCLUSION

This article proposes an adaptive tracking control law for the quadrotor aerial transportation system with variable-length cable to realize autonomous payload landing onto the mobile platform. Taking the unknown resistance coefficient into account, the proposed control law and the adaptive update law are constructed by employing the system's energy storage function. Lyapunov techniques and Barbalat's Lemma are utilized to guarantee the stability of the closed-loop system. To simulate the practical cargo delivery, a payload release task is carefully presented, which describes the process of the payload landing onto the mobile platform in detail. In the ensuing research, considering that the location of the mobile platform is often unknown prior, thus, vision-based methods will be employed to identify and predict the motion of the mobile platform. We are renovating the experimental platform to conduct outdoor experiments, which will further increase the file size and the speed of the system. Besides, considering the limitation on the amplitude of control signals, some saturated control schemes will be designed in future work.

REFERENCES

- [1] C. Zeng, H. Su, Y. Li, J. Guo, and C. Yang, "An approach for robotic leaning inspired by biomimetic adaptive control," *IEEE Trans. Ind. Informat.*, vol. 18, no. 3, pp. 1479–1488, Mar. 2022.
- [2] B. Xian and W. Hao, "Nonlinear robust fault-tolerant control of the tilt trirotor UAV under rear Servo's stuck fault: Theory and experiments," *IEEE Trans. Ind. Informat.*, vol. 15, no. 4, pp. 2158–2166, Apr. 2019.
- [3] H. Liu, Z. Liu, W. Jia, and X. Lin, "Remaining useful life prediction using a novel feature-attention-based end-to-end approach," *IEEE Trans. Ind. Informat.*, vol. 17, no. 2, pp. 1197–1207, Feb. 2021.
- [4] X. Wu, K. Xu, M. Lei, and X. He, "Disturbance-compensation-based continuous sliding mode control for overhead cranes with disturbances," *IEEE Trans. Autom. Sci. Eng.*, vol. 17, no. 4, pp. 2182–2189, Oct. 2020.
- [5] M. Chen, K. Yan, and Q. Wu, "Multiapproximator-based fault-tolerant tracking control for unmanned autonomous helicopter with input saturation," *IEEE Trans. Syst., Man, Cybern. Syst.*, vol. 52, no. 9, pp. 5710–5722, Sep. 2021.
- [6] W. He, T. Meng, S. Zhang, Q. Ge, and C. Sun, "Trajectory tracking control for the flexible wings of a micro aerial vehicle," *IEEE Trans. Syst., Man, Cybern. Syst.*, vol. 48, no. 12, pp. 2431–2441, Dec. 2018.
- [7] H.-J. Ma, Y. Liu, T. Li, and G.-H. Yang, "Nonlinear high-gain observer-based diagnosis and compensation for actuator and sensor faults in a quadrotor unmanned aerial vehicle," *IEEE Trans. Ind. Informat.*, vol. 15, no. 1, pp. 550–562, Jan. 2019.

- [8] H. Guo and J. Liu, "UAV-enhanced intelligent offloading for Internet of Things at the edge," *IEEE Trans. Ind. Informat.*, vol. 16, no. 4, pp. 2737–2746, Apr. 2020.
- [9] L. Sun, L. Wan, and X. Wang, "Learning-based resource allocation strategy for industrial IoT in UAV-enabled MEC systems," *IEEE Trans. Ind. Informat.*, vol. 17, no. 7, pp. 5031–5040, Jul. 2021.
- [10] M. A. Khan et al., "A provable and privacy-preserving authentication scheme for UAV-enabled intelligent transportation systems," *IEEE Trans. Ind. Informat.*, vol. 18, no. 5, pp. 3416–3425, May 2022.
- [11] Y. Zou, H. Zhang, and W. He, "Adaptive coordinated formation control of heterogeneous vertical takeoff and landing UAVs subject to parametric uncertainties," *IEEE Trans. Cybern.*, vol. 52, no. 5, pp. 3184–3195, May 2022.
- [12] H. Lee and H. J. Kim, "Constraint-based cooperative control of multiple aerial manipulators for handling an unknown payload," *IEEE Trans. Ind. Informat.*, vol. 13, no. 6, pp. 2780–2790, Dec. 2017.
- [13] J. Liang, Y. Chen, N. Lai, B. He, Z. Miao, and Y. Wang, "Low-complexity prescribed performance control for unmanned aerial manipulator robot system under model uncertainty and unknown disturbances," *IEEE Trans. Ind. Informat.*, vol. 18, no. 7, pp. 4632–4641, Jul. 2022.
- [14] K. Sreenath, T. Lee, and V. Kumar, "Geometric control and differential flatness of a quadrotor UAV with a cable-suspended load," in *Proc. IEEE 52nd Conf. Decis. Control*, 2013, pp. 2269–2274.
- [15] S. Tang, V. Wüest, and V. Kumar, "Aggressive flight with suspended payloads using vision-based control," *IEEE Robot. Autom. Lett.*, vol. 3, no. 2, pp. 1152–1159, Apr. 2018.
- [16] G. Yu, D. Cabecinhas, R. Cunha, and C. Silvestre, "Aggressive maneuvers for a quadrotor-slung-load system through fast trajectory generation and tracking," *Auton. Robots*, vol. 46, pp. 499–513, 2022.
- [17] B. Xian, S. Wang, and S. Yang, "An online trajectory planning approach for a quadrotor UAV with a slung payload," *IEEE Trans. Ind. Electron.*, vol. 67, no. 8, pp. 6669–6678, Aug. 2020.
- [18] Z.-Y. Lv, S. Li, Y. Wu, and Q.-G. Wang, "Adaptive control for a quadrotor transporting a cable-suspended payload with unknown mass in the presence of rotor downwash," *IEEE Trans. Veh. Technol.*, vol. 70, no. 9, pp. 8505–8518, Sep. 2021.
- [19] X. Liang, H. Lin, P. Zhang, S. Wu, N. Sun, and Y. Fang, "A nonlinear control approach for aerial transportation systems with improved antiswing and positioning performance," *IEEE Trans. Autom. Sci. Eng.*, vol. 18, no. 4, pp. 2104–2114, Oct. 2021.
- [20] L. Qian and H. H. Liu, "Path-following control of a quadrotor UAV with a cable-suspended payload under wind disturbances," *IEEE Trans. Ind. Electron.*, vol. 67, no. 3, pp. 2021–2029, Mar. 2020.
- [21] A. Akhtar, S. Saleem, and J. Shan, "Path invariant controllers for a quadrotor with a cable-suspended payload using a global parameterization," *IEEE Trans. Control Syst. Technol.*, vol. 30, no. 5, pp. 2002–2017, Sep. 2022.
- [22] W. Liu, M. Chen, and P. Shi, "Fixed-time disturbance observer-based control for quadcopter suspension transportation system," *IEEE Trans. Circuits Syst. I: Regular Papers*, vol. 69, no. 11, pp. 4632–4642, Nov. 2022.
- [23] V. P. Tran, F. Santoso, M. A. Garrat, and S. G. Anavatti, "Neural network-based self-learning of an adaptive strictly negative imaginary tracking controller for a quadrotor transporting a cable-suspended payload with minimum swing," *IEEE Trans. Ind. Electron.*, vol. 68, no. 10, pp. 10258–10268, Oct. 2021.
- [24] M. Zare, F. Pazooki, and S. E. Haghighi, "Hybrid controller of Lyapunov-based and nonlinear fuzzy-sliding mode for a quadrotor slung load system," *Eng. Sci. Technol., Int. J.*, vol. 29, 2022, Art. no. 101038.
- [25] B. Hu and S. Mishra, "Time-optimal trajectory generation for landing a quadrotor onto a moving platform," *IEEE/ASME Trans. Mechatronics*, vol. 24, no. 2, pp. 585–596, Apr. 2019.
- [26] A. Rodriguez-Ramos, C. Sampedro, H. Bavle, P. De La Puente, and P. Campoy, "A deep reinforcement learning strategy for uav autonomous landing on a moving platform," *J. Intell. Robot. Syst.*, vol. 93, no. 1, pp. 351–366, 2019.
- [27] D. Falanga, A. Zanchettin, A. Simovic, J. Delmerico, and D. Scaramuzza, "Vision-based autonomous quadrotor landing on a moving platform," in *Proc. IEEE Int. Symp. Saf., Secur. Rescue Robot.*, 2017, pp. 200–207.
- [28] J. Lin, Y. Wang, Z. Miao, H. Zhong, and R. Fierro, "Low-complexity control for vision-based landing of quadrotor UAV on unknown moving platform," *IEEE Trans. Ind. Informat.*, vol. 18, no. 8, pp. 5348–5358, Aug. 2022.
- [29] W. Zhao, H. Liu, and X. Wang, "Robust visual servoing control for quadrotors landing on a moving target," *J. Franklin Inst.*, vol. 358, no. 4, pp. 2301–2319, 2021.
- [30] S. Grzonka, G. Grisetti, and W. Burgard, "A fully autonomous indoor quadrotor," *IEEE Trans. Robot.*, vol. 28, no. 1, pp. 90–100, Feb. 2012.
- [31] S. Tang and V. Kumar, "Mixed integer quadratic program trajectory generation for a quadrotor with a cable-suspended payload," in *Proc. IEEE Int. Conf. Robot. Autom.*, 2015, pp. 2216–2222.
- [32] J. Zeng, P. Kotaru, M. W. Mueller, and K. Sreenath, "Differential flatness based path planning with direct collocation on hybrid modes for a quadrotor with a cable-suspended payload," *IEEE Robot. Autom. Lett.*, vol. 5, no. 2, pp. 3074–3081, Apr. 2020.
- [33] X. Liang, H. Yu, Z. Zhang, H. Liu, Y. Fang, and J. Han, "Unmanned aerial transportation system with flexible connection between the quadrotor and the payload: Modeling, controller design and experimental validation," *IEEE Trans. Ind. Electron.*, vol. 70, no. 2, pp. 1870–1882, Feb. 2023.
- [34] J. Huang, H. Tao, Y. Wang, and J.-Q. Sun, "Suppressing UAV payload swing with time-varying cable length through nonlinear coupling," *Mech. Syst. Signal Process.*, vol. 185, 2023, Art. no. 109790.
- [35] D. Mellinger and V. Kumar, "Minimum snap trajectory generation and control for quadrotors," in *Proc. IEEE Int. Conf. Robot. Autom.*, 2011, pp. 2520–2525.
- [36] M. Li, H. Chen, and R. Zhang, "An input dead zones considered adaptive fuzzy control approach for double pendulum cranes with variable rope lengths," *IEEE/ASME Trans. Mechatronics*, vol. 27, no. 5, pp. 3385–3396, Oct. 2022.
- [37] S. Wang, H. Zhang, S. Baldi, and R. Zhong, "Leaderless consensus of heterogeneous multiple Euler-Lagrange systems with unknown disturbance," *IEEE Trans. Autom. Control*, to be published, doi: 10.1109/TAC.2022.3172594.
- [38] B. Wei, F. Xiao, F. Fang, and Y. Shi, "Velocity-free event-triggered control for multiple Euler-Lagrange systems with communication time delays," *IEEE Trans. Autom. Control*, vol. 66, no. 11, pp. 5599–5605, Nov. 2021.
- [39] D. Li, S. S. Ge, W. He, C. Li, and G. Ma, "Distributed formation control of multiple Euler-Lagrange systems: A multilayer framework," *IEEE Trans. Cybern.*, vol. 52, no. 5, pp. 3325–3332, May 2022.
- [40] H. K. Khalil, *Nonlinear Systems*. Upper Saddle River, NJ, USA: Prentice-Hall, 2002.
- [41] F. A. Goodarzi, D. Lee, and T. Lee, "Geometric adaptive tracking control of a quadrotor unmanned aerial vehicle on SE(3) for agile maneuvers," *J. Dyn. Syst., Meas., Control*, vol. 137, no. 9, 2015, Art. no. 091007.
- [42] F. Kendoul, "Nonlinear hierarchical flight controller for unmanned rotorcraft: Design, stability, and experiments," *J. Guid., Control, Dyn.*, vol. 32, no. 6, pp. 1954–1958, 2009.
- [43] B. Zhao, B. Xian, Y. Zhang, and X. Zhang, "Nonlinear robust adaptive tracking control of a quadrotor UAV via immersion and invariance methodology," *IEEE Trans. Ind. Electron.*, vol. 62, no. 5, pp. 2891–2902, May 2015.
- [44] J.-J. E. Slotine and W. Li, *Applied Nonlinear Control*, vol. 199, no. 1. Englewood Cliffs, NJ, USA: Prentice-Hall 1991.



Hai Yu (Student Member, IEEE) received the B.S. degree in automation from Jilin University, Changchun, China, in 2020. He is currently working toward the Ph.D. degree in control science and engineering with the Institute of Robotics and Automatic Information System, Nankai University, Tianjin, China.

His research interests include nonlinear control of unmanned aerial vehicles.



Xiao Liang (Member, IEEE) received the B.S. degree in intelligence science and technology from the Hebei University of Technology, Tianjin, China, in 2013 and the Ph.D. degree in control theory and control engineering from Nankai University, Tianjin, China, in 2018.

He is currently an Associate Professor with the Institute of Robotics and Automatic Information System, Nankai University. His research interests include motion planning and nonlinear control of unmanned aerial vehicle systems.



Jianda Han (Member, IEEE) received the Ph.D. degree in mechatronic engineering from the Harbin Institute of Technology, Harbin, China, in 1998.

From 1998 to 2003, he was a Visiting Scientist with the City University of Hong Kong, Hong Kong; Michigan State University, East Lansing, MI, USA; and Cornell University, Ithaca, NY, USA. He is currently a Professor with the Institute of Robotics and Automatic Information System, Nankai University, Tianjin, China. His research interests include nonlinear estimation and control, robotics, and mechatronics systems.



Yongchun Fang (Senior Member, IEEE) received the B.S. and M.S. degrees in control theory and applications from Zhejiang University, Hangzhou, China, in 1996 and 1999, respectively, and the Ph.D. degree in electrical engineering from Clemson University, Clemson, SC, USA, in 2002.

From 2002 to 2003, he was a Postdoctoral Fellow with the Sibley School of Mechanical and Aerospace Engineering, Cornell University, Ithaca, NY, USA. He is currently a Professor with the Institute of Robotics and Automatic Information System, Nankai University, Tianjin, China. His research interests include nonlinear control, visual servoing, control of underactuated systems, and atomic force microscopy (AFM)-based nanosystems.

Dr. Fang was the recipient of the National Science Fund for Distinguished Young Scholars of China. He was an Associate Editor for the *ASME Journal of Dynamic Systems, Measurement, and Control*.